Technical University of Denmark



Damping in Digital Twins for Offshore Wind Turbine Jacket Foundations

Master thesis

17 July 2025

Author

Kasper Vang Bengtsson s203628

DTU Construct

Department of Civil and Mechanical Engineering

Project type: Master thesis (MSc) **ECTS** point: 30 Project period: 6th of January 2025 - 17th of July 2025 Author: Kasper Vang Bengtsson s203628 **Education:** Civil Engineering University: Technical University of Denmark (DTU) Department: Department of Civil and Mechanical Engineering Jan Becker Høgsberg, Associate Professor Advisor: Department of Civil and Mechanical Engineering External supervisor: Dawid Augustyn, Rambøll

Kasper Vang Bengtsson

S203628

Date

17/7-2025

Preface

This masters thesis was prepared by Kasper Vang Bengtsson in fulfilment of the requirements for the MSc in Civil Engineering at the Technical University of Denmark (DTU). The work was carried out from 6 January 2025 to 17 July 2025 and is worth 30 ECTS credits.

The study investigates the development of digital twins based on Operational Modal Analysis data, with particular emphasis on estimating and modelling damping arising from soilpile interaction using viscoelastic representations.

The project was supervised by Associate Professor Jan Becker Høgsberg, with Postdoc Mikkel Tandrup Steffensen serving as co-supervisor. It was conducted in close collaboration with Rambøll, where Dawid Augustyn served as the external supervisor.

I would like to begin by thanking Jan Becker Høgsberg for all his help throughout this thesis. His passion for his work, and for this project in particular, is clearly evident and truly inspiring. He always made time when it was needed, and I am very grateful for that.

I would also like to thank Mikkel Tandrup Steffensen for all his support throughout the project, particularly during the final phase involving model updating.

Last but not least, I would like to thank Dawid Augustyn and the team at Rambøll Copenhagen for their assistance with the internal tools and software used in this thesis; their support was invaluable.



Abstract

This thesis is part of the Hybrid Wind project which aims to reduce operation and maintenance costs in the wind energy sector through the use of digital twins (DT). The project focuses on modeling and estimating damping in wind turbines, with particular emphasis on soil damping by representing the interaction between the pile and the soil using viscoelastic models.

This thesis develops a DT in a Python environment. The DT is a simplified finite element model implemented in Python and derived from a more detailed finite element model built in ROSAP by Rambøll (ROSAP is Rambøll's program for offshore structural analysis). ROSAP together with the aeroelastic program LACFLEX is used to run time domain simulations that provide response data representing the behavior of the "physical asset" in a DT. Operational Modal Analysis (OMA) using the Stochastic Subspace Identification covariance driven algorithm is applied to these simulated responses to extract modal parameters. The extracted parameters are then used to update and calibrate the Python finite element DT.

An updating scheme is then presented to update the stiffness (k) and damping (c) parameters of the viscoelastic model to match the natural frequency and damping of the model parameters estimated by OMA of the ROSAP model, where both the viscoelastic Kelvin-Voigt model and the Standard Linear Solid model also referenced as the Zener model are used to emulate the soil-pile interaction of the offshore wind turbine.

From the findings in this thesis, it can be concluded that the viscoelastic models can be used to represent the model parameters of the ROSAP model from the OMA analysis for the first 3 natural frequencies and the damping ratio of the first mode. However, the updating scheme used in this thesis should be used with consideration of what parameters of the viscoelastic model are realistic, as the system has many possible ways to create the complex eigenvalues and there is the risk of getting correct complex eigenvalues but unrealistic undamped natural frequencies, which will result in a wrong representation of the actual system.

List of abbreviations

BR Balanced Realization

CVA Canonical Variate Analysis

DLC Design Load Case

DOF Degree Of Freedom

DT Digital Twin

EMA Experimental Modal Analysis

EOM Equation Off Motion

FE Finite Element

LTI Linear Time-Invariant

MAC Modal Assurance Criterion

MDOF Multi Degree Of Freedom

NFA Natural Frequency Analysis

OMA Operational Modal Analysis

OWT Offshore Wind Turbines

RNA Rotor-Nacelle Assembly

SDOF Single Degree Of Freedom

SLS Standard Linear Solid

SSI Stochastic Subspace Identification

SSI-Cov Stochastic Subspace Identification Covariance-driven

SVD Singular Value Decomposition

TP Transition Piece

ULS Ultimate Limit State

The terms ROSAP and LACFLEX are used throughout the thesis. These refer to two programs used at Rambøl for respectively structural offshore analysis (ROSAP) and aeroelastic simulations (LACFLEX).

Throughout this report, AI tools such as ChatGPT were used for grammar correction and to improve phrasing and clarity.



List of figures

3.1	SDOF system (Kelvin-Voigt model) with spring (k) , viscous coefficient (c) ,	
	lumped mass (m) , external load $(f(t))$, and displacement $(x(t))$	6
3.2	Free vibration of underdamped ($\zeta = 0.1$), critically damped ($\zeta = 1$) and	
	overdamped system $(\zeta = 2)$	8
3.3	The geometric of the OWT jacket foundations in 2D plane. The RNA is	
	represented as a larger node at the top	14
4.1	Stress strain curves for (a) a purely elastic material (no energy loss) and (b)	
	a viscoelastic material (showing a hysteresis loop) by harmonic loading	17
4.2	Classical linear viscoelastic models and their idealized responses, in terms of	
	stress relaxation and creep behavior. A, D, and G represent the Maxwell	
	model. B, E, and H represent the Kelvin-Voigt model. C, F, and I represent	
	the Zener model. μ is equivalent to the elastic modulus E in the text. σ is	
4.0	the stress in the model and ε is the stain [21]	20
4.3	SDOF system for the Zener model with initial spring (k_0) , viscous coefficient	
	(c), additional spring (k_1) , lumped mass (m) , external load $(f(t))$, and dis-	0.1
۲ 1	placement $(x(t))$	21
5.1	The general geometry of the jacket OWT	24 26
5.2 5.3	PILBEA, spring and dashpot system for the jacket OWT	$\frac{20}{27}$
5.4	Free decay, for the final run of an iterative process of tuning the damping	21
0.4	parameters for the tower of the OWT	28
5.5	Acceleration time series for the top node at the RNA for x and y direction.	$\frac{20}{29}$
5.6	Comparison of the jacket structure between (a) the FE Python model and (b)	20
0.0	the ROSAP model	30
5.7	Added mass to the jacket in form of (a) marine growth and (b) water from	
	flooded element, where the element with code F are flooded with water	31
5.8	The jacket structure with TP of (a) the FE Python model and (b) the ROSAP	
	model	32
5.9	The jacket structure with TP of (a) the mass density distribution and (b) the	
	modulus of elasticity distribution	32
	The full jacket OWT of (a) the FE Python model and (b) the ROSAP model.	33
	The first five mode shapes for the FE Python model	34
5.12	The first five shapes for the ROSAP model	34
6.1	Stabilization diagram for frequency across model order	41
6.2	Stabilization diagram for damping ratio as function of frequency	42
7.1	The jacket OWT with the viscoelastic model as support, where (a) has a	40
0.1	Kelvin Voigt model and (b) has a Zener model	43
8.1	Natural frequency versus damping coefficient (c) for the Zener model with	40
0.0	constant (k_1) and (k_2)	48
8.2	Surface plot of the cost function for the Kelvin-Voigt model, showing three different optimal values obtained from distinct initial guesses	49
	umereni opilitai varues obiameu mom ulstillet illitiai guesses	43

8.3	Surface plot of the cost function for the Kelvin-Voigt model, with a close up	
	of point 1 from Figure 8.2	50
8.4	Root locus plots for the Kelvin-Voigt models mode 1 of the optimized systems,	
	where (a) uses the stiffness (k) from point 1, and (b) uses the stiffness (k)	
	from point 2. The red triangle represents the optimal point. Note that only	
	the Kelvin-Voigt damping is included. The global Rayleigh damping matrix	
	is set to 0	51
8.5	Sensitivity analysis at point 1 showing the effect of $\pm 50\%$ changes in (a) base stiffness (b) (b) demains coefficient (c) and (c) secondary stiffness (b) with	
	stiffness (k_0) , (b) damping coefficient (c) , and (c) secondary stiffness (k_1) , with	E 9
0.6	all other parameters held constant.	53
8.6	Sensitivity analysis at point 2 showing the effect of $\pm 50\%$ changes in (a) base	
	stiffness (k_0) , (b) damping coefficient (c) , and (c) secondary stiffness (k_1) , with	
. -	all other parameters held constant.	55
8.7	Root locus plots for the Zener models mode 1 of the optimized systems, where	
	(a) uses the stiffness (k_0) and (k_1) from point 1, and (b) uses the stiffness (k_0)	
	and (k_1) from point 2. The red triangle represents the optimal point. Note	
	that only damping from the Zener model is included. The global Rayleigh	
	damping matrix is set to 0	55
11.1	Stabilization diagram for frequency across model order, close up for the first	
	two modes.	62
11.2	Acceleration time series for the top node at the $77m$ for x and y direction	63
11.3	Acceleration time series for the top node at the $41m$ for x and y direction	63
11 4	Acceleration time series for the top node at the TP for y and y direction	63

List of tables

3.1	Benchmark of analytical versus FE natural frequencies for a cantilever beam.
3.2	Variables of the RNA from the ROSAP OWT
3.3	Natural frequency for the first ten modes for the initial FE model
4.1	Variables for the Zener model
5.1	Natural frequency for the first ten modes of the jacket OWT ROSAP FE
	model with pile foundation
5.2	Comparison of of the natural frequency in Hz for the jacket structure in
	Python and in ROSAP
5.3	Comparison of of the natural frequency in Hz for the jacket structure with
	TP in Python and in ROSAP
5.4	Comparison of of the natural frequency in Hz for the full jacket OWT in
	Python and in ROSAP
6.1	Final model parameters for the system
8.1	Comparison of optimized point 1 and experimental natural frequency for
	Kelvin-Voigt model
8.2	Comparison of optimized point 1 and experimental damping for mode 1 and
	2 for the Kelvin-Voigt model
8.3	Comparison of the undamped natural frequency and the natural frequency
	obtained from the complex eigenvalues of the Kelvin-Voigt model
8.4	Comparison of the two optimal point for the Zener model
8.5	Comparison of optimized point 1 and experimental natural frequencies for the
	Zener model
8.6	Comparison of optimized point 1 and experimental damping for mode 1 and
	2 for the Zener model
8.7	Comparison of optimized point 2 and experimental natural frequency for the
	Zener model
8.8	Comparison of optimized point 2 and experimental damping for mode 1 and
	4 for the Zener model

Contents

1	Intr	roduction	1
	1.1	Project context: Hybrid wind	1
	1.2	Research objectives	1
	1.3	Limitations	1
	1.4	Structure of thesis	2
2	Stat	te of the art review	3
	2.1	Damping models	3
	2.2	Implementation in digital twins and model updating	5
3	Stri	uctural dynamics and finite element modeling	6
	3.1	Single degree of freedom	6
	3.2	Multi degree of freedom	8
	3.3	Finite element method for Euler-Bernoulli beams	g
	3.3	3.3.1 Modelling assumptions	S
		3.3.2 Local element matrices	10
		3.3.3 Coordinate transformation	10
		3.3.4 Benchmark test	12
		3.3.5 Initial FE model	13
4	Dar	nping in offshore wind turbines	15
-	4.1	Structural damping	15
	4.2	Soil damping	16
	4.3	Viscoelasticity	16
	4.0	4.3.1 Introduction to viscoelastic behavior	16
		4.3.2 Maxwell model	17
		4.3.3 Kelvin-Voigt model	18
		4.3.4 Zener model	19
	4.4		21
	4.4	Single degree of freedom representing of Zener model	<i>Z</i> 1
5		jacket model in ROSAP	24
		Overview of ROSAP	25
	5.2	Natural frequency analysis	27
	5.3	LACFLEX	28
	5.4	Refining the finite element model based on ROSAP	30
6	Ope	erational modal analysis	35
	6.1	Time-domain methods	36
		6.1.1 Stochastic subspace identification covariance-driven	36
		6.1.2 pyOMA2	40
		6.1.3 Data results LACFLEX	41
7	Dig	ital twins - in house Python	43

	7.1 7.2	Kelvin-Voigt implementation	44 44
8	Mod	del updating	46
	8.1	Cost function formulation	46
	8.2	Nelder-Mead optimization	47
	8.3	Verification of the Zener model	48
	8.4	Results	49
		8.4.1 Kelvin-Voigt model	49
		8.4.2 Zener model	52
9	Con	nclusion	56
10	Futi	ure work	57
11	Apr	pendices	61
		Appendix A: Mass and stiffness matrices	61
		**	62
		Appendix C: Acceleration of tower	63

1 Introduction

Wind energy is essential for sustainable power generation, with offshore wind turbines providing access to stronger wind resources. However, the harsh marine environment creates significant maintenance challenges throughout their operational lifespan. These challenging conditions necessitate advanced monitoring and predictive maintenance strategies to ensure reliable operation. Digital Twins (DT) and Operational Modal Analysis (OMA) offer promising solutions to enhance reliability while minimizing costs. This research develops methodologies for damping identification and model updating in wind turbine digital twins.

1.1 Project context: Hybrid wind

This thesis is part of the "Hybrid Wind" project, which aims to reduce operation and maintenance costs in the wind energy sector by developing a Offshore Wind Turbine (OWT) damage detection and monitoring system using DTs. In lifetime predictions using DTs, a key parameter is the structural damping, which directly affects the response amplitude, especially during resonant type loading. The present project aims at predicting damping from ambient response data, using OMA, implementing damping models in the DT environment and formulating an model updating scheme for damping in the DTs.

1.2 Research objectives

The overall research objective is to: (i) simulate structural response data using the Finite Element (FE) program ROSAP together with Rambølls aeroelastic program LACFLEX, (ii) apply OMA to identify the structures modal parameters and soil damping characteristics, and (iii) develop a simplified 3D DT in Python incorporating viscoelastic soil models as support conditions, with model parameters updated to match those identified from the OMA results.

1.3 Limitations

This thesis focuses on the offshore jacket foundation structure, encompassing the jacket steel framework from the seabed assembly point to the pile foundation and extending up to the transition piece. Throughout this work, "jacket foundation" refers exclusively to the jacket structure itself, while the supporting elements are referenced separately as either "pile foundation" or simply "piles".

Given the focus on the jacket structure, aerodynamic considerations are given limited attention. Aerodynamic effects are mainly relevant to the Rotor-Nacelle Assembly (RNA) and wind loads rather than the jacket itself. Although the LACFLEX program does incorporate aerodynamic effects, these are only briefly discussed when introducing the ROSAP and LACFLEX software packages in Chapter 5.



This thesis was conducted within a three month industry collaboration at Rambøll, providing a valuable opportunity to learn and apply the ROSAP and LACFLEX software programs in a practical engineering environment. This industry setting naturally oriented the work toward practical software application and implementation rather than comprehensive theoretical analysis of the program's underlying computational methodologies and theoretical foundations.

During the thesis work, it was discovered late in the process that the RNA was rotating within the coordinate system to account for wind direction in LACFLEX simulations. This rotation interfered with the application of the modal assurance criterion, which could have been valuable for model updating but was discovered too late in the process and ultimately excluded.

1.4 Structure of thesis

An overview of the thesis organization is provided to clarify how the study progresses from foundational concepts to implementation and validation of damping identification and model updating techniques.

Chapter 2 reviews state of the art damping models for fixed-bottom OWTs, covering both jacket and monopile foundation systems. Current research methods and established engineering practices are examined, integration into DTs and model updating workflows is detailed, and the advantages and limitations of each approach are evaluated. The chapter concludes by identifying the damping formulations most pertinent to the present study.

In Chapters 3 and 4, the thesis builds the theoretical core of the Finite Element (FE) DT by first laying out the basic of structural dynamics and finite element modeling, covering mass and stiffness assembly, eigenanalysis for natural frequencies and mode shapes and then embedding viscoelastic damping theory into that framework by comparing Kelvin-Voigt, Maxwell, and Zener formulations and their numerical implementation in a Python FE solver.

Chapters 5 and 6 present the ROSAP and LACFELX programs used to develop a high fidelity FE model of the jacket OWT, simulate its dynamic response, and apply operational modal analysis to extract modal parameters for updating the Python based DTs. This theoretical development directly supports research objectives (i) and (ii) by providing the foundational framework for both the structural response simulations and the modal parameter identification processes.

Chapters 7 and 8 configure the DT by integrating the viscoelastic damping model introduced in Chapter 4 and calibrating its parameters using the modal characteristics extracted from the ROSAP and LACFLEX simulations in Chapter 6. This integration and calibration process directly fulfills research objective (iii) by developing the simplified 3D DT in Python with viscoelastic soil models as support conditions, with model parameters updated to match those identified from the OMA results.



2 State of the art review

Offshore Wind Turbines (OWT) are slender structures excited by wind and waves, making them prone to vibrations and fatigue. Damping governs resonant response and fatigue life, the main contributions are aerodynamic, structural (material), hydrodynamic and soil/foundation mechanisms [1]. Reliable design and life prediction require accurate quantification of these effects. Digital Twins (DT) reduce modeling uncertainty by continuously reconciling high-fidelity numerical models with structural health monitoring data. Based on findings from various research papers and articles on model updating in DTs, most studies have focused on updating different stiffness parameters, while relatively few have concentrated on updating damping parameters; hence, examining damping is key to refining the dynamic response and making the model more reliable.

2.1 Damping models

Structural damping

Structural damping refers to the inherent energy dissipation within the materials and connections of the wind turbine's tower and support structure. It arises from internal friction in the steel structure and slip or microscale yielding at bolted or welded joints.

Two standard representations are used in design and analysis. In a modal formulation, a damping ratio ζ_i is assigned to each retained mode, where ζ_i represents the modal damping ratio for the *i*-th mode. Values are tuned for the lowest global bending modes. In a Rayleigh (proportional) formulation, the structural damping matrix is written as a linear combination of mass and stiffness matrices:

$$\mathbf{C} = \alpha \,\mathbf{M} + \beta \,\mathbf{K},\tag{2.1}$$

where \mathbf{C} is the damping matrix, α is the mass-proportional damping coefficient, \mathbf{M} is the mass matrix, β is the stiffness-proportional damping coefficient, and \mathbf{K} is the stiffness matrix. The coefficients (α,β) are chosen so the model reproduces target modal damping at one or two reference modes. Both approaches are implemented in common environments, e.g., OpenFAST [2]. Structural damping is typically set to 1–2% of critical damping [3].

Hydrodynamic damping

Hydrodynamic damping arises from energy losses in the interaction between ocean waves and the oscillating jacket members. Two mechanisms contribute: (a) quadratic drag on each member, computed via Morison's equation with drag coefficient C_d , and (b) radiation damping, in which the moving structure radiates pressure waves carrying energy away.



For fixed-bottom OWTs (monopiles, jackets), hydrodynamic damping is usually modeled as the sum of viscous (Morison) drag and radiation effects [4]. The viscous part uses the relative velocity between waves and structure:

$$F_D = \frac{1}{2} \rho C_d D |u_w - \dot{x}| (u_w - \dot{x}), \qquad (2.2)$$

where F_D is the drag force, ρ is the fluid density, C_d is the drag coefficient, D is the characteristic diameter of the structural member, u_w is the wave particle velocity, and \dot{x} is the structural velocity. This equation is often linearized to an equivalent viscous (modal) damping for analysis. Radiation is taken from linear potential flow theory as frequency-dependent added mass and radiation damping. Hydrodynamic damping ranges from 0.1% to 0.4%, which are quite low compared to other contributions of damping [4].

Soil damping

Soil damping refers to the energy dissipation that occurs in the soil structure system when dynamic loads (e.g., waves and wind) cause cyclic deformation of the foundation. There are two main mechanisms: (a) Hysteretic (material) damping, where the stress strain response of the soil is non-linear and path dependent, causing a loop in the stress strain curve and thus energy loss on each cycle, and (b) Radiation (viscous) damping, where dynamic waves generated in the soil by the vibrating foundation radiate energy away into the far field.

The soil structure interaction is typically modeled using spring dashpot configurations, as in the article *Modelling Damping Sources in Monopile-supported Offshore Wind Turbines* by Chen & Duffour (2018) [4]. In that work, soil damping was represented with a Kelvin-Voigt model distributed along the pile's vertical axis for a monopile. The stiffness was obtained from soil curves, and an equivalent dashpot coefficient was calculated.

Soil damping is estimated to be on of the largest source of damping for monopile-supported OWTs during idling and parked conditions, when aerodynamic damping is minimal [5]. For example, foundation (soil) damping can contribute on the order of 0.5–1.5% of critical damping [6]. Even though this thesis investigates damping for jacket foundations, the findings highlight the critical importance of understanding and modeling soil behavior appropriately, as accurate soil damping estimation remains a fundamental challenge across all offshore wind turbine foundations.



2.2 Implementation in digital twins and model updating

DTs for bottom-fixed OWTs are typically calibrated by matching measured and simulated modal properties. In the literature, most DTs and model-updating studies prioritize stiffness parameters, while damping is either prescribed or treated only implicitly [7]. A smaller part of research estimates damping explicitly, either through global Rayleigh coefficients or at the foundation level, often alongside soil stiffness. For monopiles [8] jointly update (α,β) with lumped mudline damping (c_0) and stiffness (k_{θ},k_u) , while related frameworks track coupled changes in stiffness and damping for support conditions [9, 10].

The relative scarcity of damping updates reflects practical identifiability challenges: modal damping ratios from Operational Modal Analysis (OMA) exhibit higher uncertainty and stronger operating state dependence than frequencies. Aerodynamic and hydrodynamic contributions vary significantly between idling and power production states and across different sea states. In contrast, the soil-pile contribution remains present in both operating states and varies more slowly over typical DT update horizons. When represented as complex mudline stiffness $\tilde{k}(\omega)$ or as viscous/hysteretic extensions to p-y springs, soil-pile interaction provides a physically interpretable parameter that directly affects response amplitudes and fatigue estimates.

Accordingly, this thesis targets soil pile interaction updating, focusing on foundation stiffness and damping within the DT framework while utilizing both frequency and damping ratio data from OMA for model updating. The approach employs viscoelastic models like the Kelvin-Voigt model to represent the soil-structure interaction behavior. Subsequently, Rayleigh damping is also included to account for the structural damping but will not be part of the updating parameters.

3 Structural dynamics and finite element modeling

Offshore Wind Turbines (OWT) are in places where they experience very high dynamic forces. These forces include wind, waves and rotating blades, which result in complex vibration behavior. It is crucial to understand and model these vibration to understand and predicting fatigue life, optimizing maintenance schedules and ensuring the overall integrity of the structures. This chapter will include the basic theories of:

- Structural dynamics
- Finite Element (FE) modeling

These subjects will be discussed within the context of OWTs, with a focus on jacket foundations. In this chapter, the fundamentals of structural dynamics will be described first as a Single Degree Of Freedom (SDOF) system and later as a Multi Degree Of Freedom (MDOF) system. The SDOF system will be described for simplicity, as an internal variable will be introduced to include viscoelastic effects in the support Degree Of Freedom (DOF) to approximate soil damping for the Zener model in Section 4.4.

3.1 Single degree of freedom

Consider the SDOF mass spring damper system shown in Figure 3.1. Applying Newton's second law yields Equation (3.1), the equation commonly know as the Equation Of Motion (EOM):

$$m\ddot{x}(t) + c\dot{x}(t) + kx(t) = f(t),$$
 (3.1)

where m, is the lumped mass of the system, k is the stiffness, c is the viscous damping coefficient and f is the external load.

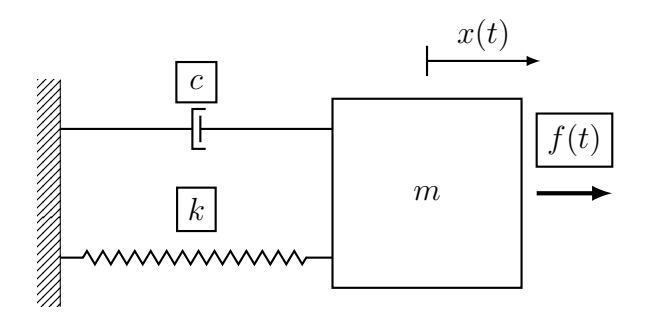


Figure 3.1: SDOF system (Kelvin-Voigt model) with spring (k), viscous coefficient (c), lumped mass (m), external load (f(t)), and displacement (x(t)).

To analyse the dynamic behavior systematically, the second-order differential equation is converted to state space form. By defining the state vector as:



$$\mathbf{x} = \begin{bmatrix} x_1 \\ x_2 \end{bmatrix} = \begin{bmatrix} x \\ \dot{x} \end{bmatrix}, \tag{3.2}$$

the equation of motion can be rewritten as a system of first-order differential equations:

$$\dot{\mathbf{x}} = \mathbf{A}\mathbf{x} + \mathbf{B}\mathbf{u} \,, \tag{3.3}$$

where:

$$\mathbf{A} = \begin{bmatrix} 0 & 1 \\ -\frac{k}{m} & -\frac{c}{m} \end{bmatrix}, \quad \mathbf{B} = \begin{bmatrix} 0 \\ \frac{1}{m} \end{bmatrix}, \quad \mathbf{u} = f(t).$$
 (3.4)

The system are determined by the eigenvalue (poles) of the systems **A** matrix, these can be obtained from:

$$\det(\mathbf{A} - \lambda \mathbf{I}) = 0, \tag{3.5}$$

where \mathbf{I} denotes the identity matrix. The solution for an underdamped system will result in 2 complex conjugates poles:

$$\lambda_{1,2} = -\zeta \omega_n \pm i\omega_n \sqrt{1 - \zeta^2} \,, \tag{3.6}$$

here ω_n is the undamped angular natural frequency and ζ is the damping ratio.

The solution to the system shown in Equation (3.6) is when the system is underdamped, meaning that $\zeta < 1$ and the response shows oscillatory behavior with exponentially decaying amplitude in free vibration [11]. If the system's damping ratio is instead $\zeta = 1$, then the system is defined as critically damped and the poles of the system become a real double root, see Equation (3.7). This leads to the fastest non-oscillatory decay:

$$\lambda_{1,2} = -\omega_n. \tag{3.7}$$

Besides the two damping behaviors described before, there is also the overdamped system where $\zeta > 1$. This leads to two distinct real poles:

$$\lambda_{1,2} = -\zeta \omega_n \pm \omega_n \sqrt{\zeta^2 - 1}. \tag{3.8}$$

The system's behavior based on the damping is illustrated in Figure 3.2, where it is shown how only the underdamped system leads to decreasing oscillatory behavior, and the over-damped and critically damped systems lead to some creep-like behavior where they decay exponentially over time [11].

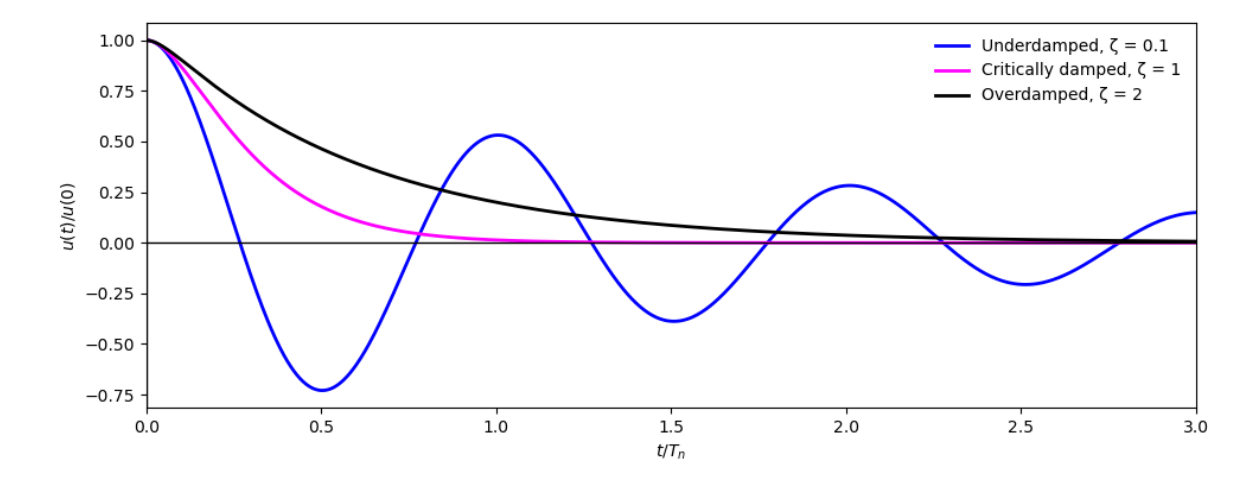


Figure 3.2: Free vibration of underdamped ($\zeta = 0.1$), critically damped ($\zeta = 1$) and over-damped system ($\zeta = 2$).

Almost all structures are by nature underdamped, which is also why they tend to oscillate when loaded by fluctuating loads. Some viscoelastic models like the Zener model do, however, include a new pole that is critically damped, which is related to the material's internal stress relaxation mechanism. This will be described more in section 4.3 and 4.4.

3.2 Multi degree of freedom

A MDOF system, such as a jacket, can be described by a second-order differential equation, similar to the one described for SDOF but in matrix form:

$$\mathbf{M}\ddot{\mathbf{x}}(t) + \mathbf{C}\dot{\mathbf{x}}(t) + \mathbf{K}\mathbf{x}(t) = \mathbf{f}(t), \tag{3.9}$$

where \mathbf{M} , \mathbf{K} and \mathbf{C} are the mass, stiffness and damping matrices, respectively. $\mathbf{q}(t)$ is the displacement and the external load is described by the vector function $\mathbf{f}(t)$. The equation of motion can be rewritten as a state space formulation, as in the case of the SDOF system, but now in matrix form. The state vector is:

$$\mathbf{x} = \begin{bmatrix} \mathbf{x} \\ \dot{\mathbf{x}} \end{bmatrix}, \tag{3.10}$$

and the system of first-order differential equations:

$$\dot{\mathbf{x}} = \mathbf{A}\mathbf{x} + \mathbf{B}\mathbf{u},\tag{3.11}$$

where:

$$\mathbf{A} = \begin{bmatrix} \mathbf{0} & \mathbf{I} \\ -\mathbf{M}^{-1}\mathbf{K} & -\mathbf{M}^{-1}\mathbf{C} \end{bmatrix}, \qquad \mathbf{B} = \begin{bmatrix} \mathbf{0} \\ \mathbf{M}^{-1} \end{bmatrix}, \qquad \mathbf{u} = \mathbf{f}(t). \tag{3.12}$$

The dynamics are governed by the eigenvalues (poles) of the systems **A** matrix exactly as in the SDOF case given in Equation (3.5). In the MDOF case, these poles are found by solving the standard eigenvalue problem:

$$(\mathbf{A} - \lambda \mathbf{I}) \mathbf{v} = \mathbf{0}, \tag{3.13}$$

where each scalar λ is a pole and \mathbf{v} its associated mode shape. For an underdamped system, each physical degree of freedom contributes one pair of complex conjugate poles (see Equation (3.6)) and the corresponding complex mode shape.

3.3 Finite element method for Euler-Bernoulli beams

The FE model that will be used in this thesis is based on 3D Euler-Bernoulli beam theory. By neglecting transverse shear deformation and rotary inertia, the kinematics reduce to the single transverse deflection w(x,t), with cross-section rotations given by $\partial w/\partial x$. This simplification is well suited to the slender jacket and tower members of offshore wind turbines. If transverse shear deformation and rotary inertia had to be included, one could apply Timoshenko beam theory, but here it's assumed that Euler-Bernoulli beam theory is sufficient.

The 3D FE model formulation is made in Python code and is an exteding of an alreade made 2D code developed by Oscar Bondo Ellekvist for the course "Dynamics of structures: theory and analysis" on DTU lectured by Professor Jan Becker Høgsberg[12].

The FE formulation is presented purely in matrix form (energy or virtual-work derivations are omitted), Only the modeling assumptions, the final local stiffness and mass matrices, the coordinate transformation procedure are summarized. The 3D formulation is based on Ferreira & Fantuzzi (2020) [13].

To properly implement the Euler-Bernoulli beam finite element formulation, specific modeling assumptions must be clearly defined. The following assumptions form the basis for all subsequent analyses in this work

3.3.1 Modelling assumptions

- 1. Prismatic, hollowshaft cross section. Sectional properties A, I_y , I_z , J (Saint-Venant torsion constant) are constant along the element of length L. Warping under torsion is neglected (no bimoment or additional warping DOF).
- 2. **Euler-Bernoulli kinematics.** Cross sections remain plane and normal to the neutral axis (zero transverse shear strains). Rotary inertia is omitted.
- 3. Linear elastic, isotropic material. Youngs modulus E and shear modulus $G = E/[2(1+\nu)]$ are constant, Poissons ratio ν enters only via G.
- 4. **Small strains and displacements.** Geometric non-linearities are not considered, strain displacement relations are linearized.



3.3.2 Local element matrices

Each two-node element carries six degrees of freedom per node:

$$\{u, w, v, \theta_x, \theta_y, \theta_z\},\$$

where u is axial displacement, w and v are the transverse deflections, θ_x is the torsion, and θ_y and θ_z are the bending rotations.

In the local (x', y', z') frame, the stiffness and mass matrices are:

$$\mathbf{K}' = [K'_{ij}]_{12 \times 12},\tag{3.14}$$

$$\mathbf{M}' = \frac{\rho AL}{420} [M'_{ij}]_{12 \times 12}. \tag{3.15}$$

The principal sub-blocks in \mathbf{K}' are:

Axial:

$$K'_{11} = \frac{EA}{L}, \quad K'_{17} = -\frac{EA}{L}.$$

Torsion:

$$K'_{44} = \frac{GJ}{L}, \quad K'_{4,10} = -\frac{GJ}{L}.$$

Bending about z':

$$\{K_{22}',K_{26}',K_{62}',K_{66}'\} = \left\{\frac{12EI_z}{L^3},\frac{6EI_z}{L^2},\frac{6EI_z}{L^2},\frac{4EI_z}{L}\right\}.$$

Bending about y':

$$\{K'_{33}, K'_{35}, K'_{53}, K'_{55}\} = \left\{\frac{12EI_y}{L^3}, -\frac{6EI_y}{L^2}, -\frac{6EI_y}{L^2}, \frac{4EI_y}{L}\right\}.$$

The mass matrix \mathbf{M}' is the consistent (continuous) form, scaled by $\rho AL/420$, with only translational inertia (rotational-DOF entries are zero) and coupling through $r_x^2 = I_x/A$. The full 12×12 local mass and stiffness matrices can be seen in Appendix 11.1.

3.3.3 Coordinate transformation

Element orientation is fixed by three nodal coordinates \mathbf{x}_1 , \mathbf{x}_2 , \mathbf{x}_3 :

- \mathbf{x}_1 , \mathbf{x}_2 carry the dynamic DOFs.
- \mathbf{x}_3 is an orientation node that, together with the line $\mathbf{x}_1 \to \mathbf{x}_2$, defines the local y'-z' plane.

Following Ferreira & Fantuzzi (2020) [13], the 3×3 rotation matrix **r** from global (x,y,z) to local (x',y',z') is assembled as:

$$\mathbf{r} = R_{\alpha} R_{\beta} R_{\gamma},\tag{3.16}$$

where

$$L = \|\mathbf{x}_2 - \mathbf{x}_1\|, \quad C_{xx'} = \frac{x_2 - x_1}{L}, \quad C_{yx'} = \frac{y_2 - y_1}{L}, \quad C_{zx'} = \frac{z_2 - z_1}{L},$$

using these relations, the rotation matrices can be assembled.

(a) Rotation about global z-axis by γ :

$$R_{\gamma} = \begin{bmatrix} \cos \gamma & \sin \gamma & 0 \\ -\sin \gamma & \cos \gamma & 0 \\ 0 & 0 & 1 \end{bmatrix},$$

where

$$\cos \gamma = \frac{C_{xx'}}{\sqrt{C_{xx'}^2 + C_{yx'}^2}}, \quad \sin \gamma = \frac{C_{yx'}}{\sqrt{C_{xx'}^2 + C_{yx'}^2}}.$$

(b) Rotation about new y-axis by β :

$$R_{\beta} = \begin{bmatrix} \cos \beta & 0 & -\sin \beta \\ 0 & 1 & 0 \\ \sin \beta & 0 & \cos \beta \end{bmatrix},$$

where

$$\cos \beta = \sqrt{C_{xx'}^2 + C_{yx'}^2}, \quad \sin \beta = -C_{zx'}.$$

(c) Optional twist about local x'-axis by α (set $\alpha = 0$ unless a non-circular section requires a prescribed spin):

$$R_{\alpha} = \begin{bmatrix} 1 & 0 & 0 \\ 0 & \cos \alpha & -\sin \alpha \\ 0 & \sin \alpha & \cos \alpha \end{bmatrix}.$$

Embedding \mathbf{r} into the twelve-DOF element gives:

$$T = \operatorname{diag}(\mathbf{r}, \mathbf{r}, \mathbf{r}, \mathbf{r}), \tag{3.17}$$

where $\operatorname{diag}(\cdot)$ indicates a diagonal matrix. The global element matrices follow by:

$$\mathbf{K}_{\text{elem}} = \mathbf{T}^T \mathbf{K}' \mathbf{T}, \quad \mathbf{M}_{\text{elem}} = \mathbf{T}^T \mathbf{M}' \mathbf{T}.$$

This transformation ensures that the local element formulation is properly oriented in the global coordinate system. The resulting global matrices \mathbf{K}_{glob} and \mathbf{M}_{glob} can then be assembled into the overall system matrices using standard finite element procedures.



3.3.4 Benchmark test

To verify that the three dimensional beam finite element formulation is implemented correctly, a benchmark test is carried out on a hollow circular cantilever beam. The cantilever is chosen because closed form expressions for its natural frequencies are available for the three principal vibration types: bending, torsion and longitudinal (axial) modes, see Inman (2001)[14]. These analytical solutions provide reference values against which the numerical eigen frequencies obtained from the FE model can be compared.

For an Euler-Bernoulli cantilever the natural bending frequencies are:

$$\omega_n^{(b)} = \frac{\beta_n^2}{L^2} \sqrt{\frac{EI}{\rho A}}, \qquad n = 1, 2, 3, \dots,$$
 (3.18)

where E is Young's modulus, I the second moment of area, ρ the material density, A the cross–sectional area, and $\beta_n L = 1.8751, 4.6941, 7.8548, 10.9955, ...$ for the first four modes. For the Longitudinal bending modes the frequencies are:

$$\omega_n^{(\ell)} = \frac{(2n-1)\pi}{2L} \sqrt{\frac{E}{\rho}}, \qquad n = 1, 2, 3, \dots,$$
 (3.19)

and the torsional natural frequencies:

$$\omega_n^{(t)} = \frac{(2n-1)\pi}{2L} \sqrt{\frac{G\gamma}{\rho I_p}}, \qquad n = 1, 2, 3, \dots,$$
 (3.20)

where G is the shear modulus, γ is the torsion constant (St. Venant), and I_p is the polar moment of inertia. Note for a hollow circular shaft $\gamma = I_p$.

The benchmark tests are conducted for a cantilever beam discretized with ten elements oriented in three dimensional space to validate the transformation matrix as well as the mass and stiffness matrices.

Table 3.1: Benchmark of analytical versus FE natural frequencies for a cantilever beam.

Mode type	mode	$\omega_n^{\rm analytical} [{\rm rad/s}]$	$\omega_n^{\rm FE} [{\rm rad/s}]$	Error [%]
Bending	1	35.487	35.488	0.003
Torsion	1	504.577	505.111	0.106
Longitudinal	1	812.446	813.306	0.106

From Table 3.1, it can be observed that the 3D FE formulation is valid for the first mode of each of the three mode types. A comprehensive table showing the first ten modes is presented in the appendix, demonstrating that the FE implementation performs as expected.



3.3.5 Initial FE model

An initial FE model was made to set up the jacket foundation OWT. It was made purely from the structural drawings from ROSAP, which will be introduced in Chapter 5. The geometry of the jacket was set up for later use so it could be used for model updating. Therefore, in the initial FE model, all material properties like the mass density ($\rho = 7850 \, \frac{\text{kg}}{\text{m}^3}$) and Young's modulus ($E = 210 \, \text{GPA}$) are set to standard values for steel structures, which will later be revised.

A lumped representation of the Rotor-Nacelle Assembly (RNA) is attached to the tower top node. The combined influence of the RNA and the blades is modelled by super imposing a 6×6 consistent mass matrix at that node. The matrix was provided by the PhD Student Mads Greve Pedersen [15] and are shown in Equation (3.21):

$$\mathbf{M}_{\text{RNA}} = \begin{bmatrix} m & 0 & 0 & 0 & ma_z & -ma_y \\ 0 & m & 0 & -ma_z & 0 & ma_x \\ 0 & 0 & m & ma_y & -ma_x & 0 \\ 0 & -ma_z & ma_y & I_{xx} + m(a_y^2 + a_z^2) & I_{xy} - ma_x a_y & I_{xz} - ma_x a_z \\ ma_z & 0 & -ma_x & I_{xy} - ma_x a_y & I_{yy} + m(a_x^2 + a_z^2) & I_{yz} - ma_y a_z \\ -ma_y & ma_x & 0 & I_{xz} - ma_x a_z & I_{yz} - ma_y a_z & I_{zz} + m(a_x^2 + a_y^2) \end{bmatrix}$$
(3.21)

where m is the total mass of the RNA, a_x, a_y, a_z are the offsets of its centre of gravity from the node along the global x, y, and z axes and $I_{xx}, I_{yy}, I_{zz}, I_{xy}, I_{xz}, I_{yz}$ are the corresponding components of the inertia tensor evaluated about that centre of gravity. The coupling inertias (xy, xz, and yz) are not included in this FE model as they were not included in the ROSAP model and they are set to 0 in this thesis. The variables used for the lumped RNA are shown in Table 3.2, which are taking from ROSAP.

Table 3.2: Variables of the RNA from the ROSAP OWT.

m [kg]	$a_x [m]$	a_y [m]	a_z [m]	$I_{xx} [kg \cdot m^2]$	$I_{yy} [kg \cdot m^2]$	$I_{zz} [kg \cdot m^2]$
80.9×10^4	-3.5	0	4	4.84×10^{8}	2.78×10^{8}	2.79×10^{8}

The geometry of the jacket OWT foundations can be seen in Figure 3.3, where the larger point node is representing the RNA at the top node.



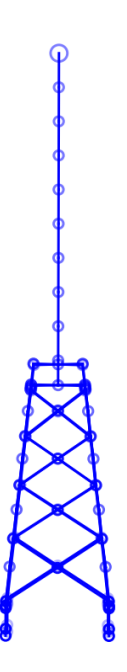


Figure 3.3: The geometric of the OWT jacket foundations in 2D plane. The RNA is represented as a larger node at the top.

Solving the undamped eigenvalue problem the first ten natural frequency of the structure can be determinate and are shown in Table 3.3.

Table 3.3: Natural frequency for the first ten modes for the initial FE model.

Mode	1	2	3	4	5	6	7	8	9	10
Freq. [Hz]	0.142	0.144	0.504	0.697	0.761	0.976	1.068	1.318	1.657	2.176

The natural frequencies shown in Table 3.3 are from the initial setup of the jacket OWT, before the material density (ρ) and Young's modulus (E) are updated to match the FE model from ROSAP.

4 Damping in offshore wind turbines

Damping governs how quickly free vibrations decay and, therefore, directly influences fatigue accumulation, ultimateload amplification, and the serviceability of Offshore Wind Turbines (OWT). Four mechanisms dominate:

- Structural damping: Energy dissipated within the steel tower, transition piece, and welded joints.
- Hydrodynamic damping: Energy lost to water drag and small waves generated by the motion of the jackets submerged members.
- Aerodynamic damping: Energy absorbed by the rotating blades as they resist and smooth out tower swaying
- Soil damping: Energy lost in the seabed as the piles cyclically deform and radiate ground waves.

Only structural damping and soil damping will be explained here as it is the only considered in the DTs implementation later in Chapter 7.

4.1 Structural damping

Structural damping in OWTs is commonly modeled using Rayleigh damping, where the damping matrix C is formulated as a linear combination of the mass and stiffness matrices:

$$\mathbf{C} = \alpha \mathbf{K} + \beta \mathbf{M},\tag{4.1}$$

where α and β can be calculated in different ways depending on what the suit the system the best. One of the most common way is to set a minimum damping ratio for the first frequency:

$$\alpha = \zeta_{min}\omega_{min} , \ \beta = \zeta_{min}/\omega_{min}, \tag{4.2}$$

where ζ_{min} and ω_{min} is the minimum damping ratio and natural angular frequency respectively. Normally ζ_{min} is set to 1-2% critical [3]. Here the ζ_{min} is set to 1% for when the digital twin is set up in Chapter 7. A damping ratio of 1 % was chosen because it is the standard implementation in the program ROSAP, which will be introduced later in Chapter 5 and it aligns with the literature.



4.2 Soil damping

Soil damping denotes the energy that is dissipated in the seabed when the jacket piles deform cyclically under wind, wave and operational loads. In present day offshore wind design practice this mechanism is captured with non-linear soil reaction curves that link pile displacement to soil resistance. The lateral response is represented by p-y curves, while axial shaft and tip responses are described by t-z and q-z curves, respectively.

Because these springs are non-linear, loading and unloading do not follow the same path every cycle therefore encloses a hysteresis loop and part of the input energy is lost as heat and tiny rearrangements of the soil grains. The same curves that provide static stiffness thus deliver damping automatically in a fully non-linear time-domain model. When the curves are linearised for example for modal or frequency domain analysis the hysteretic effect disappears and an equivalent damping ratio can be added to the system.

This thesis will model the damping from the soil with a linear viscoelasticity material at the support instead, were the initial stiffness from the soil curves can be used to estimate the stiffness parameters in the viscoelastic model, which will be described in the next section.

4.3 Viscoelasticity

As noted in Section 4.2, this thesis focuses on representing soil damping by adding a linear viscoelastic support at the jacket foundation. The aim is to capture energy dissipation with the simplest possible model, deliberately excluding the non-linear soil-curve effects discussed in the same section.

4.3.1 Introduction to viscoelastic behavior

Viscoelastic materials exhibit both elastic (instantaneous, recoverable) and viscous (time-dependent, dissipative) response when deformed. Unlike a purely elastic solid, a viscoelastic materials stressstrain relationship depends on time (or, equivalently, on loading frequency).

Three key manifestations of viscoelasticity are: creep, stress relaxation, and hysteresis. Creep refers to the gradual increase in strain under a sustained constant stress, for example, a polymer or soil sample under a steady load will slowly deform over time. Stress relaxation is the complementary effect, if a material is suddenly strained to a fixed level and held, the stress needed to maintain that strain will decrease (relax) with time. Hysteresis denotes the energy dissipation observed in cyclic loading-unloading, typically visible as a loop in the stressstrain curve, the area of the loop represents energy lost per cycle. It should be noted that this loop forms a perfect ellipse only when the material is subjected to a purely harmonic load. These phenomena are illustrated in Figure 4.1, which contrasts a purely elastic material no hysteresis, stress and strain in phase with a viscoelastic material showing a hysteresis loop and phase lag.



Viscoelastic behavior is common in polymers, biological tissues, metals at high temperature, and soils in all cases, part of the deformation energy is dissipated internally due to time-dependent micro-mechanisms (e.g. polymer chain motion, internal friction in soil) rather than fully stored elastically [16].

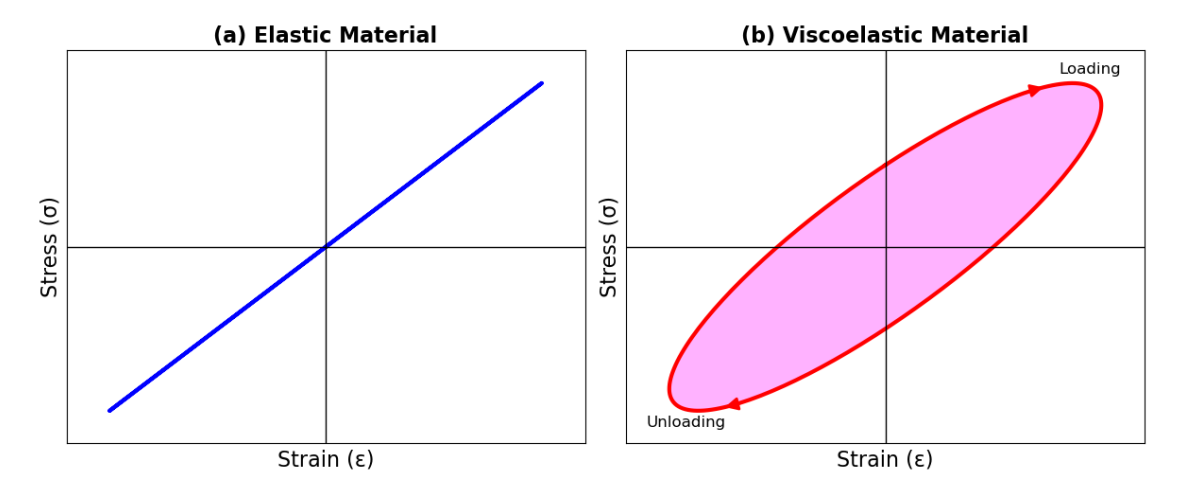


Figure 4.1: Stress strain curves for (a) a purely elastic material (no energy loss) and (b) a viscoelastic material (showing a hysteresis loop) by harmonic loading.

The simplest linear elements used to model viscoelastic materials are the ideal spring obeying Hookes law, $\sigma = E\varepsilon$ and the ideal dashpot a viscous damper obeying, $\sigma = \eta\dot{\varepsilon}$. By combining these elements, several classical rheological models can be constructed. Figure 4.2 illustrates three fundamental models the Maxwell model, Kelvin-Voigt model, and Standard Linear Solid (SLS) model along with their characteristic creep and relaxation responses. Each model comprises a particular arrangement of springs and dashpots and yields a distinct stressstrain constitutive law and time-dependent behavior.

4.3.2 Maxwell model

The Maxwell model represents the simplest configuration for capturing viscoelastic behavior, consisting of a linear elastic spring (elastic modulus E) and a viscous dashpot (viscosity η) arranged in series, as illustrated in Figure 4.2 A. In this arrangement, both elements experience identical stress while their respective strains are additive. The governing constitutive equation is derived from the series configuration:

$$\dot{\varepsilon}(t) = \frac{\dot{\sigma}(t)}{E} + \frac{\sigma(t)}{\eta},\tag{4.3}$$

where $\dot{\varepsilon}$ is the total strain rate, $\dot{\sigma}$ is the rate of change of stress, σ is the stress. This indicates that the total strain rate comprises contributions from both elastic deformation and viscous flow [17].



Creep behavior

When subjected to constant stress σ_0 , the Maxwell model demonstrates unbounded deformation. The spring responds instantaneously with strain $\varepsilon(0^+) = \sigma_0/E$, while the dashpot subsequently exhibits continuous viscous flow, resulting in linearly increasing strain over time. This behavior reveals a fundamental limitation: the absence of an elastic deformation limit under sustained loading. This is illustrated in Figure 4.2 D.

Stress relaxation

During stress relaxation experiments, where a sudden strain ε_0 is applied and maintained, the Maxwell model predicts complete stress decay according to:

$$\sigma(t) = \sigma_0 \exp(t/\tau),\tag{4.4}$$

where $\tau = \eta/E$ represents the characteristic relaxation time [17]. This exponential decay continues until the stress reaches zero, indicating the model's inability to sustain long-term loads. This is illustrated in Figure 4.2 G.

Limitations

A critical limitation of the Maxwell model is its inability to exhibit elastic recovery. Any deformation accumulated in the dashpot remains permanent, as the model lacks memory of its reference configuration. Consequently, this model is unsuitable for representing solid materials that demonstrate complete recovery, though it effectively describes fluid-like behavior or materials exhibiting significant permanent deformation.

4.3.3 Kelvin-Voigt model

The Kelvin-Voigt model, employs a parallel arrangement of spring and dashpot elements see Figure 4.2 B. This configuration ensures equal strain in both components ($\varepsilon_{total} = \varepsilon_{spring} = \varepsilon_{dashpot}$) while stresses are additive [18]. The constitutive relationship is expressed as:

$$\sigma(t) = E\varepsilon(t) + \dot{\eta}\varepsilon(t), \tag{4.5}$$

which describes the total stress as the sum of the elastic term $E\varepsilon(t)$ and the viscous term $\eta\dot{\varepsilon}(t)$.

Creep behavior

Under constant applied stress σ_0 , the Kelvin-Voigt model exhibits bounded creep behavior. Initial deformation is prevented by the dashpot's resistance to instantaneous strain. Subsequently, the material deforms gradually according to:

$$\varepsilon(t) = \frac{\sigma_0}{E} (1 - \exp(-\frac{t}{\tau})), \tag{4.6}$$



where $\tau = \eta/E$ s the relaxation time constant. Over time, the material deforms asymptotically toward a maximum strain of σ_0/E at which point all stress is supported by the spring element alone. Unlike the Maxwell model's unlimited flow, the Kelvin-Voigt model exhibits this bounded deformation, characteristic of solid-like behavior [18]. This is illustrated in Figure 4.2 E.

Stress relaxation

A significant limitation emerges during stress relaxation: when strain is held constant $(\dot{\varepsilon} = 0)$, the dashpot contributes no stress, leaving only the spring's elastic response $\sigma = E\varepsilon_0$. Consequently, the model predicts no stress relaxation, maintaining constant stress indefinitely. This is illustrated in Figure 4.2 H.

Recovery and energy dissipation

Despite its limitations in stress relaxation, the Kelvin-Voigt model demonstrates complete recovery upon load removal, returning to its original configuration. However, this recovery is time-dependent due to dashpot resistance. Under cyclic loading, the model generates elliptical hysteresis loops characteristic of linear viscous damping, with energy dissipation increasing proportionally with loading frequency.

4.3.4 Zener model

The Standard Linear Solid (SLS), also known as the Zener model, represents the simplest configuration capable of exhibiting both bounded creep and partial stress relaxation. The model consists of a Maxwell element (spring E_2 in series with dashpot η) arranged in parallel with an additional spring E_1 see Figure 4.2 C. The governing differential equation relates stress and strain through:

$$\sigma(t) + \frac{\eta}{E_2} \dot{\sigma}(t) = E_1 \varepsilon(t) + \frac{\eta (E_1 + E_2)}{E_2} \dot{\varepsilon}(t). \tag{4.7}$$

This formulation incorporates two elastic moduli (E_1 and E_2), one viscosity parameter (η), and introduces the characteristic relaxation time $\tau = \eta/E_2$ [19].

Creep behavior

When subjected to constant stress σ_0 , the SLS model exhibits a characteristic two-stage response. At the instant of loading, the material demonstrates an immediate elastic strain of $\varepsilon(0^+) = \sigma_0/(E_1 + E_2)$, where both spring elements contribute to the initial stiffness due to the dashpot's resistance to instantaneous deformation. Subsequently, the material undergoes time-dependent creep as the Maxwell arm gradually deforms, allowing the strain to increase exponentially toward its asymptotic value of $\varepsilon(\infty) = \sigma_0/E_1$. This creep behavior follows the relationship:

$$\varepsilon(t) = \frac{\sigma_0}{E_1} - \frac{\sigma_0 E_2}{E_1 (E_1 + E_2)} \exp(-t/\tau),$$
(4.8)



where the exponential term represents the transient response that decays with the characteristic time constant $\tau = \eta(E_1 + E_2)/E_1E_2$ [20]. This is illustrated in Figure 4.2 F.

Stress relaxation

The SLS model's response to a suddenly applied and maintained strain ε_0 reveals its ability to partially relax stress over time. Initially, both springs resist the deformation, generating a stress of $\sigma(0^+) = (E_1 + E_2)\varepsilon_0$. As time progresses, the dashpot in the Maxwell arm permits gradual flow, allowing the spring E_2 to release its stress while spring E_1 maintains a constant contribution. Consequently, the stress decays exponentially from its initial value to a non-zero equilibrium stress of $\sigma(\infty) = E_1\varepsilon_0$, following:

$$\sigma(t) = E_1 \varepsilon_0 + E_2 \varepsilon_0 \exp(-t/\tau), \tag{4.9}$$

where $\tau = \eta/E_2$ [20]. This partial relaxation distinguishes the SLS from both the Maxwell model (which relaxes completely) and the Kelvin-Voigt model (which shows no relaxation). This is illustrated in Figure 4.2 I.

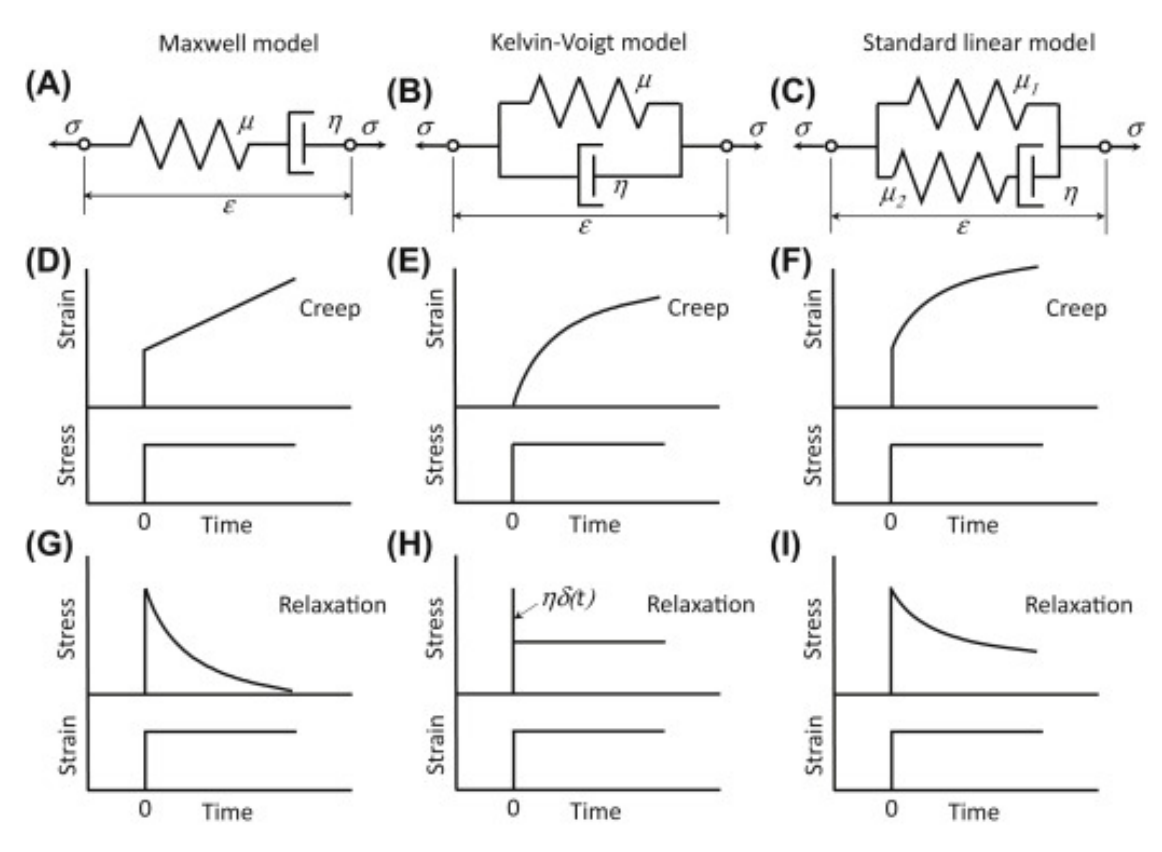


Figure 4.2: Classical linear viscoelastic models and their idealized responses, in terms of stress relaxation and creep behavior. A, D, and G represent the Maxwell model. B, E, and H represent the Kelvin-Voigt model. C, F, and I represent the Zener model. μ is equivalent to the elastic modulus E in the text. σ is the stress in the model and ε is the stain [21].

4.4 Single degree of freedom representing of Zener model

As described in Section 4.3, the Zener model, is one of the simplest rheological representations that reproduces both stress relaxation and creep. It comprises a Maxwell branch, a dashpot with viscosity (c) in series with a spring of stiffness (k_1) acting in parallel with a purely elastic spring of stiffness (k_0) . This thesis will therefore model the support with a Zener model instead of a simple support. Here the Zener model will be introduced trough a Single Degree Off Freedom (SDOF) system likewise to the SDOF descibed Section 3.1 which was a Kelvin-Voigt model. The system is illustrated in Figure 4.3 where a Zener model is attach to a lumped mass (m).

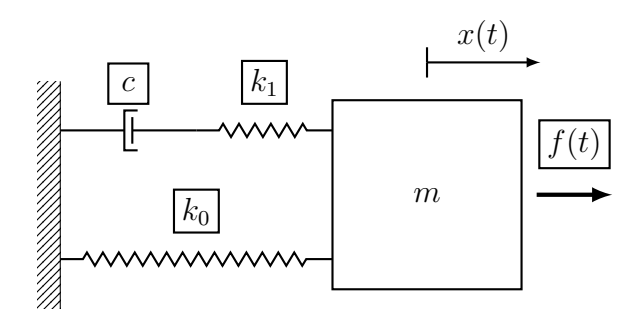


Figure 4.3: SDOF system for the Zener model with initial spring (k_0) , viscous coefficient (c), additional spring (k_1) , lumped mass (m), external load (f(t)), and displacement (x(t)).

When adding the Maxwell branch instead of only the dashpot, an additional state variable z is introduced. This variable describes the relationship between the dashpot c and the spring k_1 in that branch. The internal force z serves as the state variable and must be identical for both the dashpot and the spring. For the single translational DOF x(t) of mass m the equation of motion becomes:

$$m\ddot{x} + k_0 x + z = f(t),$$
 (4.10)

$$\dot{z} + \Omega z = k_1 \dot{x},\tag{4.11}$$

where z(t) is an internal force that is present only in the Maxwell branch and $\Omega = \frac{k_1}{c}$. Introducing the state vector:

$$\mathbf{x} = \begin{bmatrix} x & \dot{x} & z \end{bmatrix}^T, \tag{4.12}$$

which yields the first-order system:

$$\frac{d}{dt} \underbrace{\begin{bmatrix} x \\ \dot{x} \\ z \end{bmatrix}}_{\mathbf{X}} = \underbrace{\begin{bmatrix} 0 & 1 & 0 \\ -\frac{k_0}{m} & 0 & -\frac{1}{m} \\ 0 & k_1 & -\Omega \end{bmatrix}}_{\mathbf{A}} \mathbf{x} + \underbrace{\begin{bmatrix} 0 \\ \frac{1}{m} \\ 0 \end{bmatrix}}_{\mathbf{B}} \mathbf{f}_{\text{ext}}(t). \tag{4.13}$$

The matrix **A** governs the coupled motion of the physical displacement, its velocity and the viscoelastic internal coordinate.

For the homogeneous system $\dot{\mathbf{x}} = \mathbf{A} \mathbf{x}$ the characteristic polynomial reads:

$$\det(\lambda \mathbf{I} - \mathbf{A}) = \lambda^3 + \Omega \lambda^2 + \frac{k_0 + k_1}{m} \lambda + \frac{k_0 \Omega}{m} = 0,$$
(4.14)

with $\Omega = k_1/c$. Positive m, k_0 , k_1 , c imply all coefficients in (4.14) are positive, there are three roots: two complex conjugated poles and one real negative pole:

$$\lambda_{1,2} = -\omega_n \pm i \omega_d, \qquad \lambda_3 \approx -\Omega.$$
 (4.15)

The system has two complex conjugate poles representing an oscillatory, exponentially decaying mode and one purely real negative pole representing a non oscillatory viscoelastic relaxation mode. To express the undamped natural frequency ω_n , ω_d and the third pole, one would need to solve the characteristic polynomial in Equation (4.14), but this is a complex problem and is not done in this thesis. Instead, an example using values for the SDOF Zener model is shown by solving the eigenvalue problem of the state matrix **A**.

To emulate the OWT described in the Chapter 5, the lumped mass (m) in the Zener model is chosen as the modal mass of the first mode after normalizing the mode shape to unity at maximum deflection. The stiffness k_0 is then selected so that $f_0 = \frac{1}{2\pi} \sqrt{\frac{k_0}{m}} = 0.183$ Hz, which is the first natural frequency of the OWT. The second stiffness k_1 is chosen so that $\frac{f_0}{f_{\infty}} = 1.1$, where f_{∞} is the natural frequency when $c \to \infty$. In this limit, the system frequency is $f = \frac{1}{2\pi} \sqrt{\frac{k_0 + k_1}{m}}$, as the damper becomes rigid and cannot move. The three parameters are shown in Table 4.1 with a chosen damping coefficient.

Table 4.1: Variables for the Zener model.

		. , .	$c [N \cdot s/m]$
1.12×10^6	1.48×10^{6}	3.11×10^{5}	5.00×10^4

Solving the state matrix \mathbf{A} with the parameters in Table 4.1, the three poles of the system can be calculated:

$$\lambda_{1,2} = -0.022 \pm i \, 1.153, \qquad \lambda_3 = -6.176.$$
 (4.16)

By taking the absolute value of $\lambda_{1,2}$, the undamped natural frequency can be calculated:

$$f_n = \frac{|\lambda_{1,2}|}{2\pi} = 0.1836 \,\text{Hz}.$$
 (4.17)

The third pole can be compared with Ω :

$$-\Omega = -\frac{k_1}{c} = 6.219 \approx \lambda_3. \tag{4.18}$$

From this it is shown that f_n is slightly higher than f_0 due to the Maxwell branch and the third pole is close to Ω .

5 Full jacket model in ROSAP

ROSAP is the name of Ramboll's offshore structural analysis program. It has been developed as a tool for analyzing and solving problems related to fixed offshore steel platforms. In this section, a general overview of ROSAP with regard to what has been used in this project will be described as well as the aeroelastic program LACFLEX used for simulations of aerodynamics of the tower.

The jacket Offshore Wind Turbine (OWT) used in this thesis is shown in Figure 5.1, which illustrates its general geometry. It is a generic model developed at Rambøll and slightly modified. The tower corresponds to a 15 MW turbine.

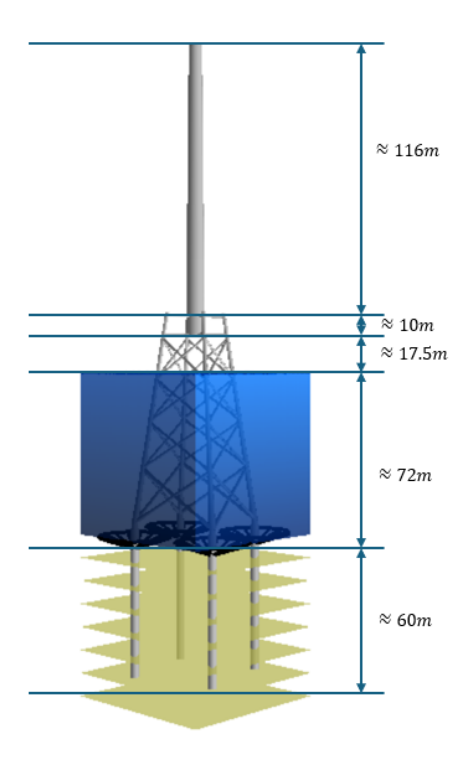


Figure 5.1: The general geometry of the jacket OWT.

The jacket itself, with the transition piece, is approximately 100 m tall. The water depth is 72 m. The piles extend 60 m into the ground, and the tower is around 116 m tall. The jacket OWT was loaded with a standard Design Load Case (DLC) 6.4, which was included in the ROSAP setup because it provided the best results. DLC 6.4 is a load case for an idling or standstill turbine in which power production is off while the structure is subjected to normal wave and wind loading.

5.1 Overview of ROSAP

ROSAP is the overall name for the analysis program, that consist of serval subprograms some which are described here. The main program ROSA is a 3D finite element program that performs static and dynamic analysis. In the context of this project only dynamic analysis are used. This allows for either determining natural frequencies of linear structures or performing time history analysis through direct integration for both linear and non-linear structures. This thesis is only analysing the jacket OWT in a linear analysis.

To simulate the wave load on the structure another subprogram is used called wavegen. It first creates a three dimensional field of waterparticle velocity, acceleration and excess pressure on a rectangular grid. For a regular sea the field is obtained from an analytical wave theory (sinusoidal, Stokes 5th or streamfunction), for an irregular sea it is built by superposing spectral components from, for example, a Pierson Moskowitz or JONSWAP spectrum, allowing waves to arrive from several directions. At each time step ROSA interpolates the grid values to every structural station and converts them to forces with Morisons equation

$$F_{\perp} = \frac{1}{2} \rho_w C_D D |U| U + \frac{\pi}{4} \rho_w C_M D^2 \dot{U}, \qquad (5.1)$$

where U and \dot{U} are the local fluid velocity and its time derivative, D is the member diameter, and C_D and C_M are the drag and inertia coefficients, respectively. Integrating F_{\perp} along the member length yields the drag and inertia forces that drive the Finite Element (FE) simulation.

To visualize the result for the different analysis the subprogram GLORIA is used. GLORIA is an user interface tool where the result can be analyses. In this thesis is primaraly used to visualize the structure with nodes and elements and also analysis the mode shape from Natural Frequency Analysis (NFA) that will be introduced in the next section. It can be used for much more e.g it is used to visualize the Ultimate Limit State (ULS) analysis with utilization of all element and see the section forces.

When running the NFA or ULS analysis in ROSA, the standard is to linearize the non-linear P-y and other soil curves to an initial stiffness constant for each element in the piles. This means that the initial setup for these analyses does not include any damping from the soil-pile interaction, and since the focus of this thesis is to add a viscoelastic model at the support to model the soil damping in a simple linear way in the Digital Twin (DT), this presents a problem.

To include damping from the soil-pile interaction, a subprogram called PILBEA is used to add a Kelvin-Voigt model to each element along the piles to include damping. The PIL-BEA subprogram is usually used when performing seismic analysis, but can also be used to simply include springs and dashpots along the piles. To include damping in the piles an equivalent viscous damping are calculated based on the first natural frequency (ω_1) and the initial linearized soil stiffness (k) form the soil curves.



Figure 5.2 shows how the PILBEA program include the Kelvin-Voigt model along the piles to include stifness and damping to the soil-pile intaraction.

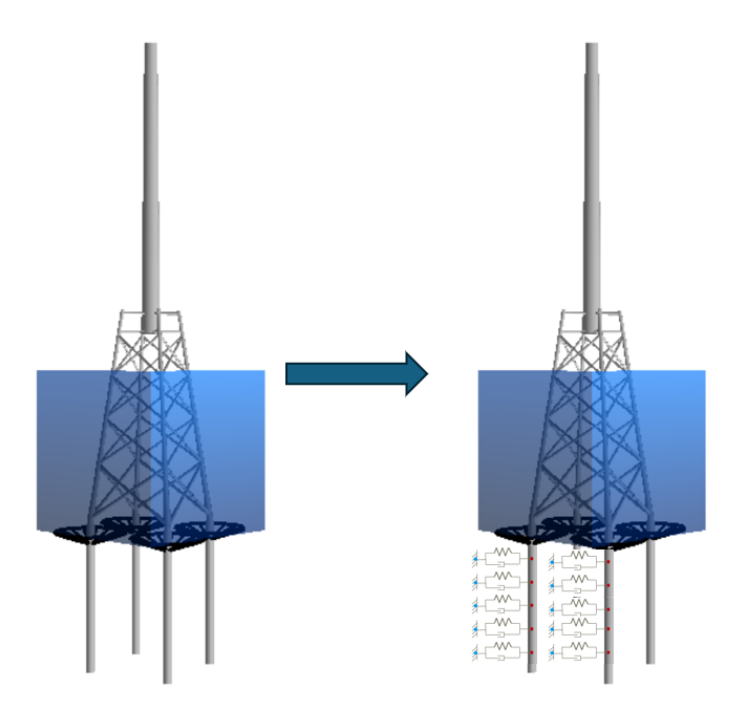


Figure 5.2: PILBEA, spring and dashpot system for the jacket OWT.

To include the damping in the pile, the theory of energy dissipation for a Kelvin-Voigt type damping mechanism is adopted [22]. The loss factor (η) is written as:

$$\eta = \omega \frac{c}{k},\tag{5.2}$$

where ω is the angular natural frequency, c is the viscous damping coefficient and k is the (linearised) stiffness of the pile-soil system. From that the equivalent viscous damping ratio can be obtained as:

$$\zeta_{eq} = \frac{\eta}{2} \frac{\omega_0}{\omega},\tag{5.3}$$

were ω_0 is the undamped natural angular frequency and ζ_{eq} is equivalent viscous damping ratio. Re-arranging the above and identifying ω_0 with the first natural frequency ω_1 of the system gives the dashpot constant used in the numerical model:

$$c = \frac{2\zeta k}{\omega_1},\tag{5.4}$$

where ζ is the target first mode damping ratio, which is set to $\zeta = 0.02$. The damping constants are then calculated for each node along the piles, using the initial stiffness from ROSAP. The damping coefficient for each element in the piles are then included in the global damping matrix.



5.2 Natural frequency analysis

In ROSAP it is possible to make an NFA, where the natural frequency of the structure are being calculated in a similar way as described in Chapter 3 with mass matrix and stiffness matrix are used to solve the undamped natural eigenvalue problem, to get the natural frequency and mode shape of the structure. In Figure 5.3 the mode shape of the first to modes and the forth mode are shown as they are the ones that will later be used in the model updating of the DT. The reason for looking at those specific modes are explained in Section 6.1.3 as it is based on the Operational Modal Analysis (OMA) from the LACFELX data which will be introduced in Section 5.3. From the NFA the first ten natural frequency are shown in Table 5.1

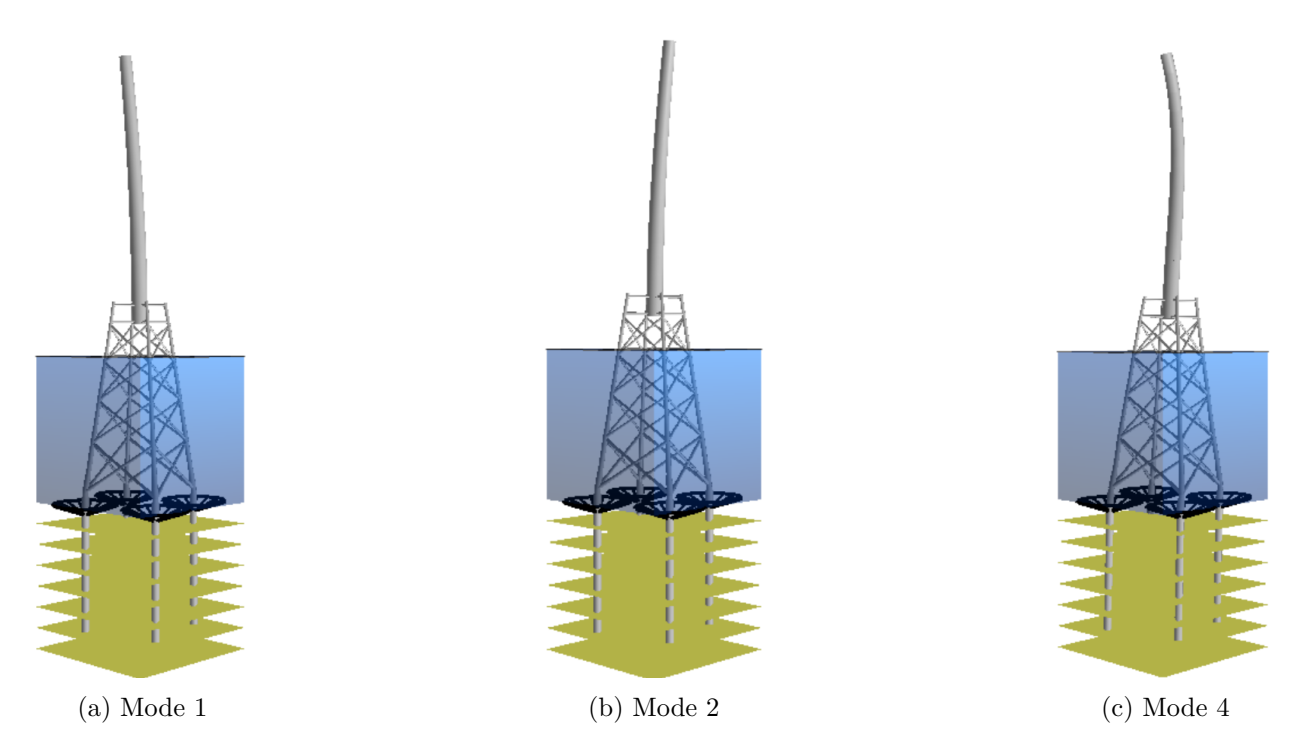


Figure 5.3: Mode shape 1, 2 and 4 for the jacket OWT, visualized in GLORIA.

Table 5.1: Natural frequency for the first ten modes of the jacket OWT ROSAP FE model with pile foundation.

Mode	1	2	3	4	5	6	7	8	9	10
Freq. [Hz]	0.183	0.186	0.595	0.760	0.805	0.960	1.088	1.268	1.723	1.978

Table 5.1 shows the ten lowest natural frequencies off the OWT jacket. All ten lie below 2 Hz, and the two lowest are below 0.2 Hz. These two modes have similar shapes (see Figure 5.3), they bend in different directions due to the placement of the RNA and blades.



5.3 LACFLEX

LACFLEX is an aeroelastic simulation program based on the FLEX5 code developed at the Technical University of Denmark (DTU). Like FLEX5, it models the dynamic behavior of wind turbines by coupling structural motion with aerodynamic loading. These types of aeroelastic programs are used to simulate how wind turbines respond to wind forces over time, taking into account both the flexibility of the structure and the changing aerodynamic conditions. LACFLEX uses blade element momentum theory to calculate aerodynamic forces on the blades and combines this with a structural model that includes the flexibility of the blades and tower. This allows for realistic time-domain simulations of wind turbine behavior under various operating conditions.

To enable simulations in the aeroelastic program LACFLEX, the structure is reduced to a superelement that can be loaded into the software. This reduction is performed using the Craig-Bampton method, a component mode synthesis technique that combines static constraint modes (representing the response to boundary displacements) with fixed interface normal modes (representing the internal dynamics of the component) [23]. The reduced model retains only the six degrees of freedom of the transition piece, plus an additional 24 fixed interface modes.

The LACFLEX setup was made from the initial ROSAP FE model with out the Kelvin-Voigt model from the PILBEA implementation and the damping on the tower was then tunes to match the 1% critical damping by changing the damping on the tower itself. This was done by a iterative process using a Python script form Rambøll that change the damping on the tower run a free decay analysis and rerun until the desired damping ratio is uptained. The final free decay run are shown in Figure 5.4 where it can be seen that the mean damping ratio is approximately 1% for both x and y direction.

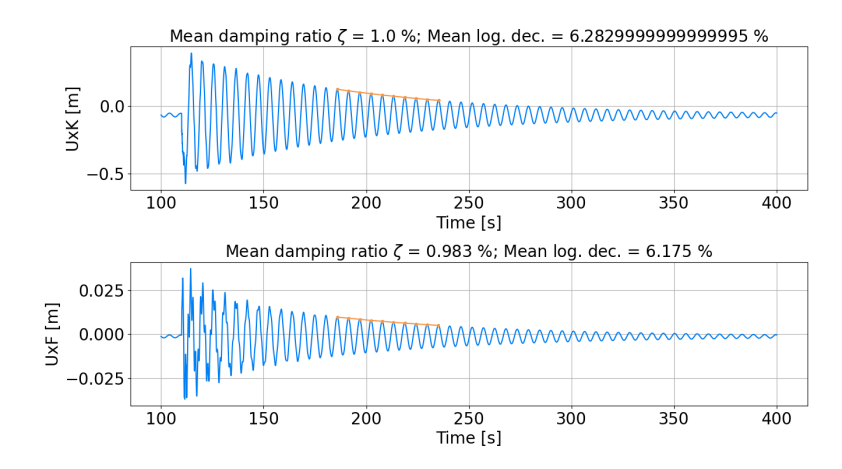


Figure 5.4: Free decay, for the final run of an iterative process of tuning the damping parameters for the tower of the OWT.

After the tuning of the tower damping to the critical damping of 1%, a ROSAP super element with the soil damping from the PILBEA implementation was inserted, so the only change in damping should come from the implementation of the Kelvin-Voigt spring/dashpot model.

From the LACFLEX simulation, acceleration at different location can be extracted. Four locations along the vertical axis are used: the top node at the RNA, two elevation along the tower and then a node at the transion piece. The acceleration data for the ten minutes are shown in Figure 5.5 for the top node at the RNA, the other three elevations are shown in Appendix 11.3.

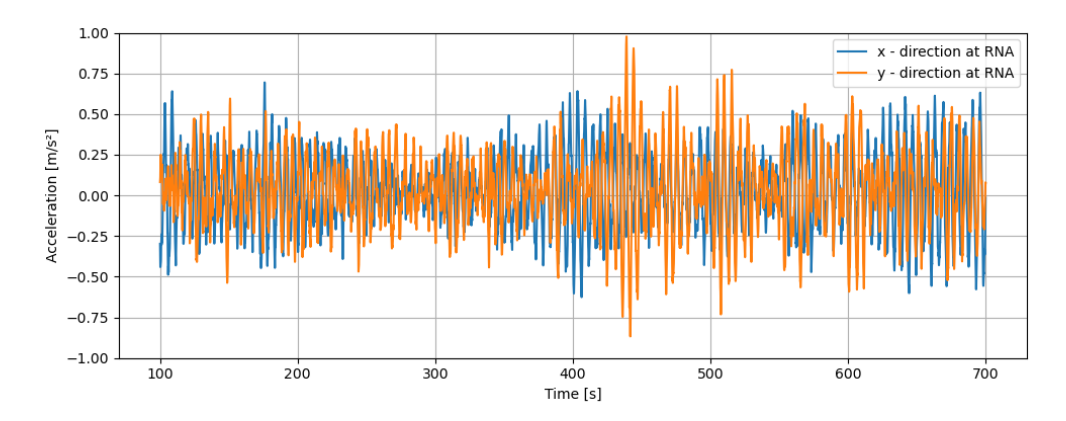


Figure 5.5: Acceleration time series for the top node at the RNA for x and y direction.

The acceleration time series are then analysed using OMA, as described in Chapter 6. The results of this analysis, including the modal parameters of the structure, are also presented in that Chapter.

5.4 Refining the finite element model based on ROSAP

As stated in Section 3.3.5, an initial FE model was created based only on the drawings of the nodes, elements, and cross sections of the jacket and tower. This FE model will now be manually updated so that the natural frequency of the FE model matches the ROSAP model, ensuring that only the parameters in the viscoelastic model will be included in the model updating scheme later in Chapter 8. To more easily compare the different parts of the jacket OWT, it is divided into three parts: the jacket alone, the jacket with the Transition Piece (TP), and the entire jacket OWT. The comparison was made with simple support in the ROSAP model to ensure the structure itself matches, as the FE model in Python is made without piles.

The first part that will be examined is the jacket by itself. Part of the jacket is underwater and ROSAP accounts for this with some added mass for the parts that are submerged under water, there is also some added mass from secondary structure and marine growth. To account for this in the FE model in Python, the mass density ρ of the jacket is increased across all elements of the jacket. This is of course not totally accurate as the ROSAP model does not uniformly add mass to the whole structure, but it is deemed sufficient for this thesis. An illustration of the jacket by itself for both Python and the ROSAP model are shown in Figure 5.6 and the marine grow on the jacket and which element are flooded with water are shown in Figure 5.7.

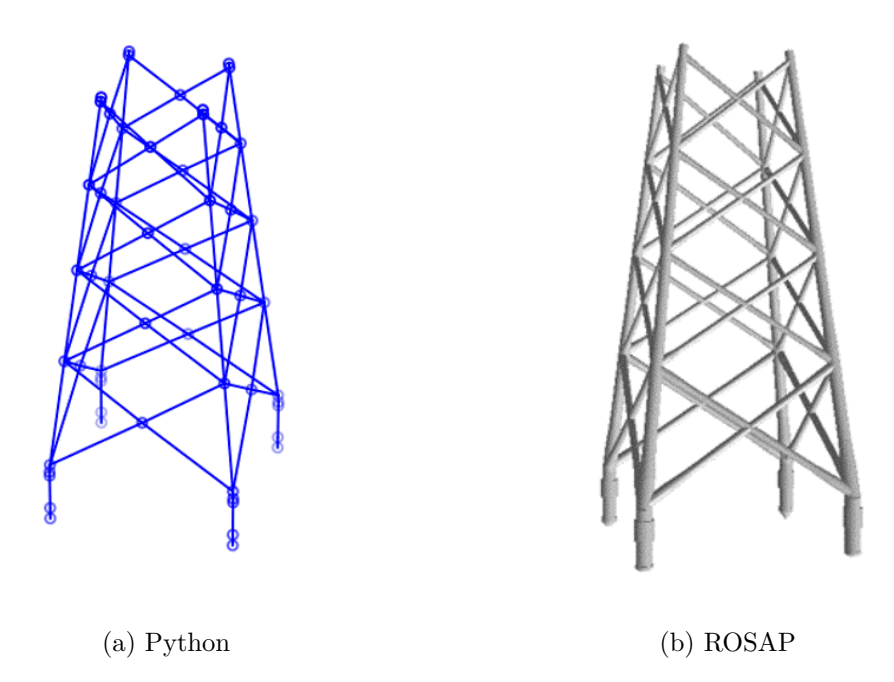


Figure 5.6: Comparison of the jacket structure between (a) the FE Python model and (b) the ROSAP model.

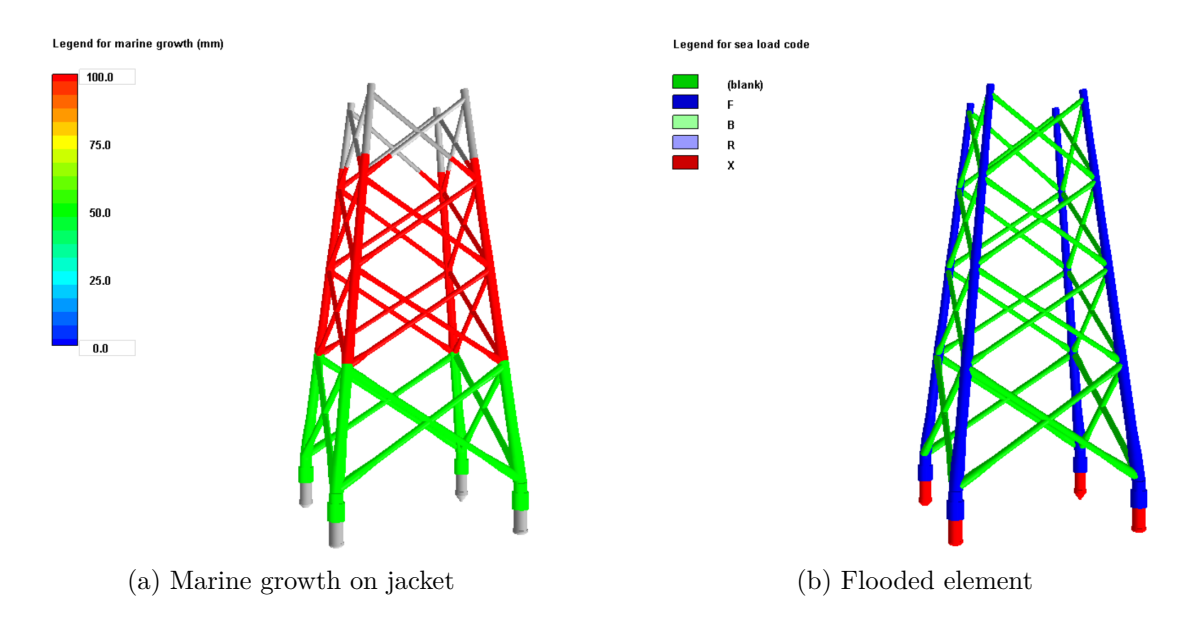


Figure 5.7: Added mass to the jacket in form of (a) marine growth and (b) water from flooded element, where the element with code F are flooded with water.

The mass density ρ of the FE model is then adjusted to match the natural frequency of the jacket from ROSAP. A comparison of the final natural frequencies of the FE jacket model in Python and in ROSAP is shown in the Table 5.2.

Table 5.2: Comparison of the natural frequency in Hz for the jacket structure in Python and in ROSAP.

	Mode 1	Mode 2	Mode 3	Mode 4	Mode 5
ROSAP	0.898	0.909	1.093	1.165	1.575
Python	0.901	0.901	1.144	1.150	1.727
Relative Error (%)	0.33	0.88	4.6	1.3	9.2

The next part is looking at the jacket with the TP. Here the ROSAP model had set the mass density ρ of the elements in the TP to 0 and added a lumped mass in the center of the TP as well as setting the Youngs modulus to 1050 GPa for the elements. To account for this in the FE model in Python, the stiffness of the elements was set to the same value and the mass density ρ of the TP elements was again changed so the natural frequency of the two models matches. An illustration of the jacket with TP for both Python and the ROSAP model are shown in Figure 5.8 and the mass density and Youngs modulus of the jacket with TP are shown in Figure 5.9.

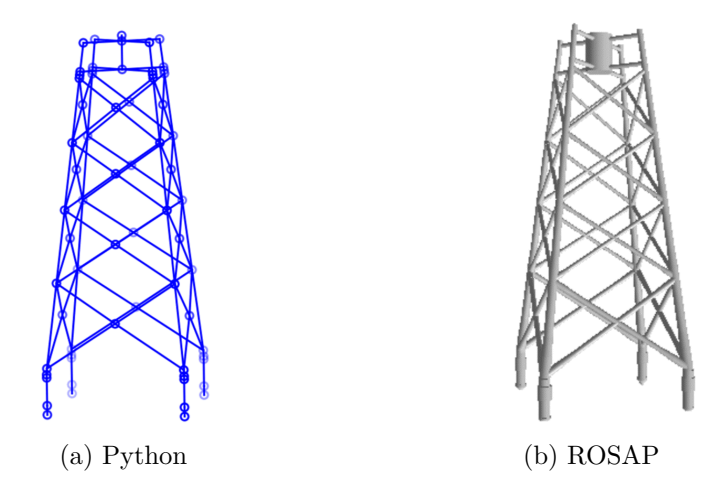


Figure 5.8: The jacket structure with TP of (a) the FE Python model and (b) the ROSAP model.

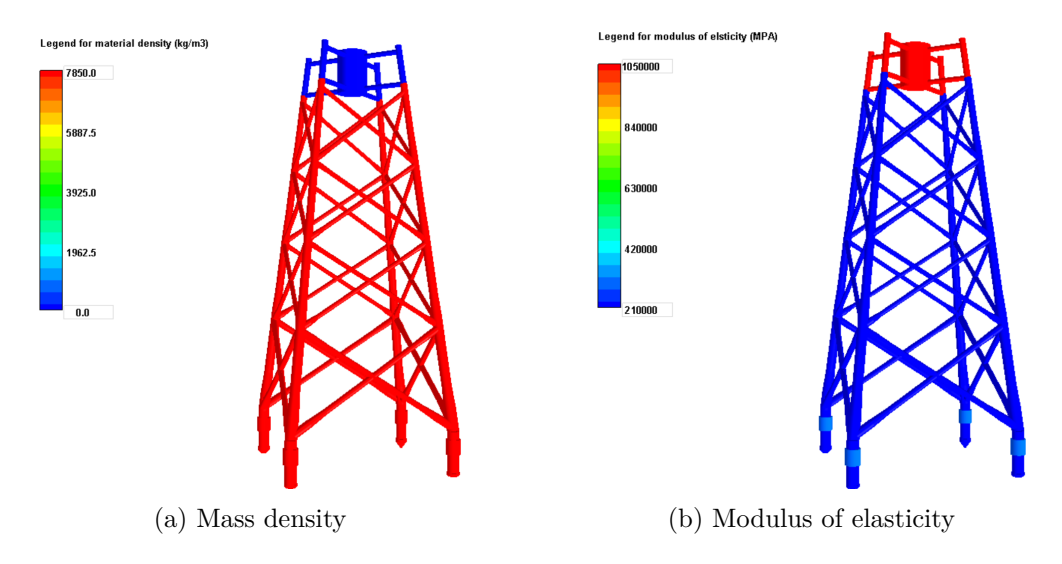


Figure 5.9: The jacket structure with TP of (a) the mass density distribution and (b) the modulus of elasticity distribution.

The comparison on the final natural frequency of the FE jacket model with TP in Python and in ROSAP are shown in Table 5.2.

Table 5.3: Comparison of the natural frequency in Hz for the jacket structure with TP in Python and in ROSAP.

	Mode 1	Mode 2	Mode 3	Mode 4	Mode 5
ROSAP	0.898	0.909	1.093	1.165	1.575
Python	0.901	0.901	1.144	1.150	1.727
Relative Error (%)	0.33	0.88	4.6	1.3	9.2



At the end, the full jacket OWT is modeled in both the FE Python model and in ROSAP, where the jacket with the TP is put together with the tower of the OWT. The only thing that has been changed from the initial model of the tower is the mass density ρ that in the initial model was set to $7850 \frac{\text{kg}}{\text{m}^3}$ and in the ROSAP model it was $8500 \frac{\text{kg}}{\text{m}^3}$. An illustration of the full jacket OWT for both Python and the ROSAP model is shown in Figure 5.10.

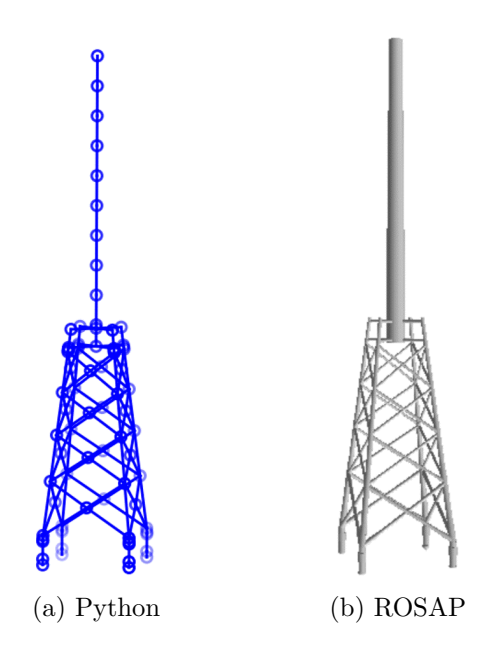


Figure 5.10: The full jacket OWT of (a) the FE Python model and (b) the ROSAP model.

The comparison on the final natural frequency of the FE full jacket OWT model in Python and in ROSAP are shown in Table 5.2.

Table 5.4: Comparison of the natural frequency in Hz for the full jacket OWT in Python and in ROSAP.

	Mode 1	Mode 2	Mode 3	Mode 4	Mode 5
ROSAP	0.1836	0.869	0.527	0.775	0.819
Python	0.183	0.186	0.572	0.749	0.794
Relative Error (%)	0.49	0.40	3.55	3.46	3.09

A comparison of the first five mode shapes between the FE Python model and the ROSAP model is made to ensure that the models not only have the same natural frequencies but also matching mode shapes. Figure 5.11 shows the first five mode shapes for the FE Python model, and Figure 5.12 shows them for the ROSAP model.

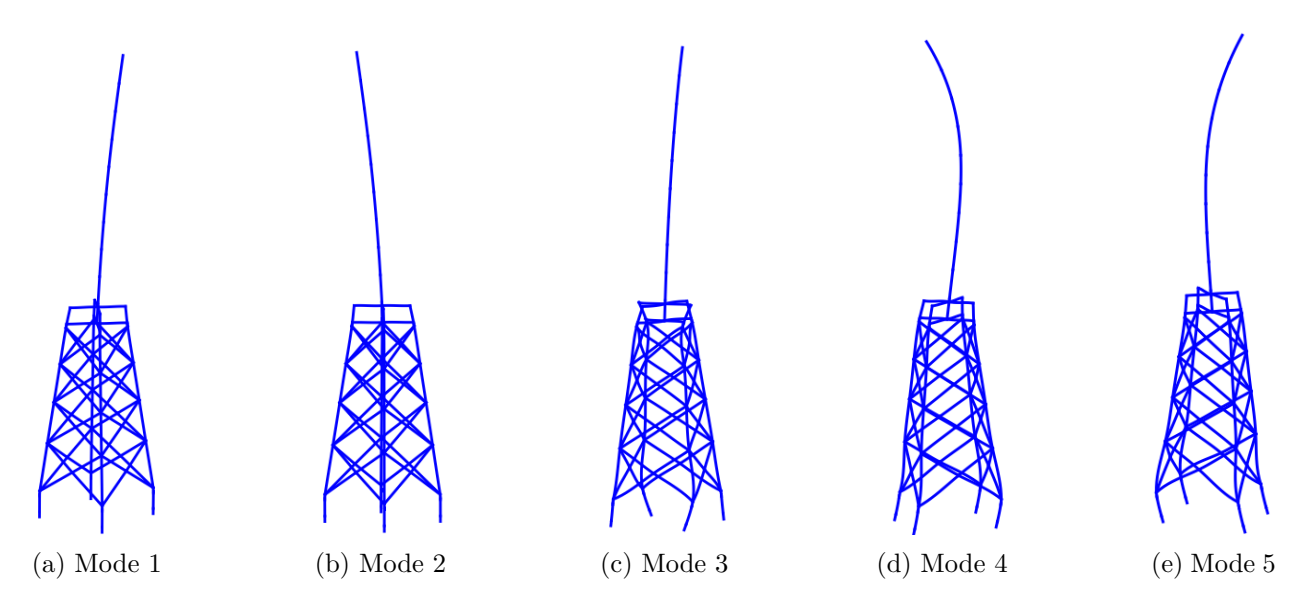


Figure 5.11: The first five mode shapes for the FE Python model.

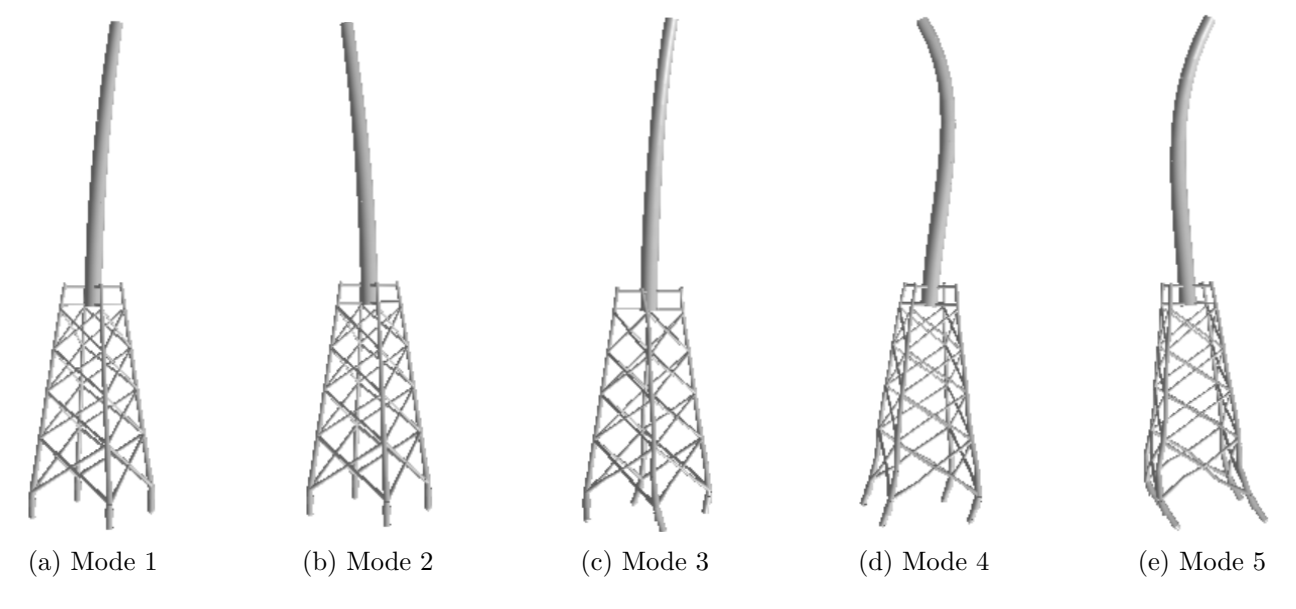


Figure 5.12: The first five shapes for the ROSAP model.

From Figures 5.11 and 5.12, it is shown that the first five mode shapes from the FE Python model and the ROSAP model are the same. The first two mode shapes are the first bending modes in each direction, the third mode shape is a torsional mode shape, and the fourth and fifth are the second mode shapes in each direction.

6 Operational modal analysis

Operational Modal Analysis (OMA) is a form of experimental vibration testing in which the modal properties of a structure are identified using only its measured response, without requiring any measured input forces. In contrast, traditional Experimental Modal Analysis (EMA) relies on known, controlled excitation forces and measured responses to determine modal parameters.

In EMA, the system is excited by shakers or impact hammers and the input-output data are used to compute frequency response functions [24], from which modal frequencies, damping, and mode shapes are extracted. OMA, on the other hand, treats the excitation as unknown (typically ambient or operational loads such as wind, waves, traffic, etc.) and uses only output measurements (e.g. vibrations) in system identification. Because the input in OMA is not measured and generally considered random, OMA algorithms are formulated in a stochastic framework modeling the excitation as a gaussian distributed random noise. For this reason, OMA is sometimes termed output-only modal analysis or ambient vibration testing [25].

OMA offers distinct practical advantages for large civil structures and Offshore Wind Turbines (OWT). EMA on large structures is challenging: Introducing measurable artificial forces to excite a full-scale wind turbine or a jacket foundation is expensive, logistically difficult, and potentially disruptive. OMA leverages natural excitation, wind, wave, and operating loads in the case of an OWT to extract modal parameters without special test setups. This means the structure can be identified under its actual in-service conditions, which is highly relevant for Digital Twin (DT) models of offshore wind turbine foundations.

A DT is a numerical model updated to reflect the real structure's behavior, using OMA, one can identify the true natural frequencies, damping ratios, and mode shapes of the jacket OWT foundation during operation, and use these to calibrate the finite element model in the DT. In essence, OMA provides in situ modal estimates that are representative of the structures current state, which improves the fidelity of the DT in predicting dynamic responses. This approach is valuable for structural health monitoring and performance assessment, as tracking changes in identified modal parameters via OMA can indicate stiffness, damping or other changes due to damage or environmental effects.

It should be noted that OMA is not without challenges. Since the excitation is not measured, identification algorithms must carefully distinguish structural modal characteristics from excitation influence. The ambient excitation is assumed to be broadband (exciting all modes of interest), if this assumption is violated (e.g. presence of narrow band harmonics or deficient frequency content), certain modes or damping estimates may be unreliable.

Nevertheless, over the past two decades OMA has become a widely accepted tool for modal identification in wind engineering and civil structures, complementing or even supplanting EMA in situations where only output data are available.

In the context of OWT, OMA enables continuous monitoring and updating of the structures modal damping in the DT during real operation, something impractical with EMA. By regularly identifying the modal parameters via OMA, the DT can be updated to ensure it predicts the behavior accurately under various operational conditions.

6.1 Time-domain methods

OMA methods are broadly categorized into frequency-domain and time-domain approaches. Frequency domain methods (such as Frequency Domain Decomposition) identify modal parameters from peaks in spectral matrices derived from measured responses. In contrast, time-domain methods work directly with time signals or their correlation functions, treating the measured response as a stochastic, Linear Time-Invariant (LTI) process while preserving phase relationships and capturing damping as explicit exponential decay [25, 24].

Among time-domain techniques, Stochastic Subspace Identification (SSI) is widely employed in structural dynamics. SSI has two main variants: Stochastic Subspace Identification Data Driven (SSI-Data), which operates directly on block Hankel matrices of measured samples, and Stochastic Subspace Identification Covariance Driven (SSI-Cov), which first compresses the data into empirical covariances before matrix factorization. While both approaches can yield similar modal parameters, they differ in computational strategy and numerical properties. Preliminary investigations for this study showed that SSI-Cov performed better for estimating damping parameters and was therefore chosen for modal identification. The theoretical background and implementation details of SSI-Cov are explained comprehensively in Section 6.1.1

6.1.1 Stochastic subspace identification covariance-driven

The SSI-Cov algorithm estimates a discrete time state space model from output-only data. The SSI-Cov algorithm are explained mainly based on the book from Rainieri & Fabbrocino (2014) [25]. The starting point is the stochastic LTI state-space description:

$$\mathbf{x}_{k+1} = \mathbf{A} \, \mathbf{x}_k + \mathbf{w}_k, \tag{6.1}$$

$$\mathbf{y}_k = \mathbf{C}\,\mathbf{x}_k + \mathbf{v}_k,\tag{6.2}$$

here \mathbf{x}_k denotes the unmeasured state vector, \mathbf{y}_k the measured response, \mathbf{A} the discrete state matrix, \mathbf{C} the discrete output matrix, and \mathbf{w}_k and \mathbf{v}_k are mutually uncorrelated, zero mean white noise sequences, representing process and measurement noise, respectively.



Given N output samples, the sample covariance at lag i is estimated by:

$$\hat{\mathbf{R}}_i = \frac{1}{N-i} \mathbf{Y}_{(1:N-i)} \mathbf{Y}_{(i:N)}^{\mathsf{T}}, \tag{6.3}$$

where $\mathbf{Y}_{(1:N-i)}$ is the data matrix with the last i samples removed and $\mathbf{Y}_{(i:N)}$ removes the first i samples. The correlations at different time lags are then assembled into whats called a Toeplitz matrix:

$$\mathbf{T}_{1|i} = \begin{bmatrix} \hat{\mathbf{R}}_i & \hat{\mathbf{R}}_{i-1} & \cdots & \hat{\mathbf{R}}_1 \\ \hat{\mathbf{R}}_{i+1} & \hat{\mathbf{R}}_i & \ddots & \hat{\mathbf{R}}_2 \\ \vdots & \vdots & \ddots & \vdots \\ \hat{\mathbf{R}}_{2i-1} & \hat{\mathbf{R}}_{2i-2} & \cdots & \hat{\mathbf{R}}_i \end{bmatrix}.$$
(6.4)

Each correlation matrix $\hat{\mathbf{R}}$ has the dimensions $l \times l$, where l is the number of channels from the investigated system. The dimension of the Toeplitz matrix then becomes $li \times li$, where i is the number of block rows. For a system of n order it has to fulfill:

$$li \ge n. \tag{6.5}$$

In practice, the systems model order n is unknown, but can be estimated by e.g looking at the peaks in power spectra density matrix in a certain range of interest and knowing outside this range the algorithm becomes less precise. In the matter of this project, only FE model are used and model order is therefore a know parameter.

With the model order in place the number of block rows i can be chosen larger or equal to n/l and is a choice the user can pick. Giving the factorization property of:

$$\mathbf{R}_i = \mathbf{C}\mathbf{A}^{i-1}\mathbf{G},\tag{6.6}$$

where G is the next state-output covariance matrix. The block Toeplitz matrix can be expressed as:

$$\mathbf{T}_{1|i} = \begin{bmatrix} \mathbf{C} \\ \mathbf{C}\mathbf{A} \\ \vdots \\ \mathbf{C}\mathbf{A}^{i-1} \end{bmatrix} [\mathbf{A}^{i-1}\mathbf{G} \ \mathbf{A}^{i-2}\mathbf{G} \ \cdots \ \mathbf{A}\mathbf{G} \ \mathbf{G}] = \mathbf{O}_{i} \mathbf{\Gamma}_{i}, \tag{6.7}$$

where it can be divided into the observability matrix:

$$\mathbf{O}_{i} = \begin{bmatrix} \mathbf{C} \\ \mathbf{C}\mathbf{A} \\ \vdots \\ \mathbf{C}\mathbf{A}^{i-1} \end{bmatrix}, \tag{6.8}$$

and the the reversed controllability matrix:

$$\Gamma_i = [\mathbf{A}^{i-1}\mathbf{G} \quad \mathbf{A}^{i-2}\mathbf{G} \cdots \mathbf{A}\mathbf{G} \quad \mathbf{G}]. \tag{6.9}$$

Provided that the *i* satisfies $i l \ge n$ and the pair (\mathbf{A}, \mathbf{C}) is observable/controllable, both \mathbf{O}_i and $\mathbf{\Gamma}_i$ are full rank *n*. Consequently, the rank of $\mathbf{T}_{1|i}$ coincides with *n*. To extract this rank from noisy data, the Singular Value Decomposition (SVD) are performed:

$$\mathbf{T}_{1|i} = \mathbf{U} \, \mathbf{\Sigma} \, \mathbf{V}^{\top} = \begin{bmatrix} \mathbf{U}_1 & \mathbf{U}_2 \end{bmatrix} \begin{bmatrix} \mathbf{\Sigma}_1 & \mathbf{0} \\ \mathbf{0} & \mathbf{0} \end{bmatrix} \begin{bmatrix} \mathbf{V}_1^{\top} \\ \mathbf{V}_2^{\top} \end{bmatrix}, \tag{6.10}$$

where Σ_1 collects the *n* significant singular values. Neglecting the noise subspace (\mathbf{U}_2 , \mathbf{V}_2 , and the zero block of Σ) corresponding singular vectors are:

$$\mathbf{T}_{1|i} = \mathbf{O}_i \mathbf{\Gamma}_i = \mathbf{U}_1 \mathbf{\Sigma}_1 \mathbf{V}_1^{\mathsf{T}},\tag{6.11}$$

here \mathbf{U}_1 and \mathbf{V}_1 contain the dominant left- and right-singular vectors, respectively, while the diagonal matrix $\mathbf{\Sigma}_1$ stores the positive singular values in descending order. By splitting this reduced SVD one obtains explicit expressions for the extended observability and the reversed controllability matrices:

$$\mathbf{O}_i = \mathbf{U}_1 \, \mathbf{\Sigma}_1^{1/2} \, \mathbf{T},\tag{6.12}$$

$$\Gamma_i = \mathbf{T}^{-1} \, \mathbf{\Sigma}_1^{1/2} \, \mathbf{V}_1^{\top}, \tag{6.13}$$

here \mathbf{T} denotes an arbitrary, invertible similarity transformation matrix for the state-space in Equation (6.1) and (6.2). Since every invertible matrix \mathbf{T} leads to an equivalent state-space model, it is convenient to set it equal to the identity matrix \mathbf{I} :

$$\mathbf{T} = \mathbf{I}.\tag{6.14}$$

Based on the definitions established for the observability matrix \mathbf{O}_i and controllability matrix $\mathbf{\Gamma}_i$ both the output influence matrix \mathbf{C} and the subsequent state-output covariance matrix \mathbf{G} can be determined. These correspond to the initial l rows of \mathbf{O}_i and the final l columns of $\mathbf{\Gamma}_i$, in that order.

There are two different way to get to the state matrix \mathbf{A} according to Rainieri & Fabbrocino (2014) [25]. One strategy exploits the decomposition of the Toeplitz matrix with a single time-lag shift, and other estimate the state matrix \mathbf{A} by exploiting the shift structure of the observability matrix. The second methods is used as it is the one used in pyOMA2, which is the tool box used to perform OMA in this thesis. The observability matrix is derived by applying invertible weighting matrices \mathbf{W}_1 and \mathbf{W}_2 to pre- and post-multiply the matrix $\mathbf{T}_{1|i}$, followed by computing the SVD of the resulting weighted Toeplitz matrix and excluding zero singular values:

$$\mathbf{O}_i = \mathbf{W}_1^{-1} \, \mathbf{U}_1 \, \mathbf{\Sigma}_1^{1/2}. \tag{6.15}$$



From that the final state matrix can be expressed as:

$$\mathbf{A} = \left(\mathbf{O}_i^{\uparrow}\right)^+ \mathbf{O}_i^{\downarrow},\tag{6.16}$$

where \mathbf{O}_i^{\uparrow} and $\mathbf{O}_i^{\downarrow}$ are \mathbf{O}_i with removing the last and first row respectively. According to Rainieri & Fabbrocino (2014)[25] there are two variants of setting the weighting matrices $(\mathbf{W}_1, \mathbf{W}_2)$ up, Balanced Realization (BR) and Canonical Variate Analysis (CVA). The CVA SSI-cov are using the Cholesky factorization of the toeplitz matrix and the BR SSI-cov are using identity matrices as weights. Here the BR SSI-cov are explained as it is the one implemented in pyOMA2. For the BR SSI-cov the weights can be expressed as:

$$\mathbf{W}_1 = \mathbf{W}_2 = \mathbf{I},\tag{6.17}$$

where **I** again is the identity matrix. In a balanced realisation, the controllability Gramian $\Gamma_i \Gamma_i^{\mathsf{T}}$ and the observability Gramian $\mathbf{O}_i^{\mathsf{T}} \mathbf{O}_i$ coincide and are both diagonal, a fact that follows directly from the orthonormality of the SVD factors \mathbf{U}_i and \mathbf{V}_i , which can be expressed as:

$$\mathbf{O}_{i}^{\mathsf{T}} \, \mathbf{O}_{i} = \, \boldsymbol{\Sigma}_{1}^{1/2} \, \mathbf{U}_{1}^{\mathsf{T}} \mathbf{U}_{1} \, \boldsymbol{\Sigma}_{1}^{1/2} = \, \boldsymbol{\Sigma}_{1} = \, \boldsymbol{\Sigma}_{1}^{1/2} \, \mathbf{V}_{1}^{\mathsf{T}} \mathbf{V}_{1} \, \boldsymbol{\Sigma}_{1}^{1/2} = \, \boldsymbol{\Gamma}_{i} \, \boldsymbol{\Gamma}_{i}^{\mathsf{T}}. \tag{6.18}$$

This shows that the realised system is both controllable and observable. In a balanced realisation, the signal transfers from the inputs to the states, and from the states to the outputs are similar and balanced [25].

From the state matrix **A** and the output matrix **C** the modal parameters of the system can be estimated as, the Eigenvalue Decomposition can be expressed as:

$$\mathbf{A} = \mathbf{\Psi} \mathbf{\Lambda} \mathbf{\Psi}^{-1}, \tag{6.19}$$

where Λ is a diagonal matrix with the eigen values λ_i and the Ψ are the eigen vectors. The eigen values are outputted as a combination of the mode shapes and the eigen value and the actual mode shape can be found by:

$$\mathbf{\Phi} = \mathbf{D}\mathbf{\Psi}.\tag{6.20}$$

The natural frequency f, and the damping ratio ζ can then be expressed as:

$$f_i = \frac{|\ln(\lambda_i)|}{2\pi\Delta t},\tag{6.21}$$

$$\zeta_i = -\frac{\operatorname{Re}(\ln(\lambda_i))}{|\ln(\lambda_i)|}.$$
(6.22)

In practice, measurement noise and computational errors can introduce spurious modes in the identified modal parameters. To distinguish between physical modes and mathematical artifacts, stabilization diagrams are employed. These diagrams plot identified modes across different model orders, where true physical modes appear as stable vertical lines while spurious modes show inconsistent behavior.



By examining the consistency of natural frequencies, damping ratios, and mode shapes across increasing model orders, the actual system parameters can be reliably extracted from the noisy identification results.

6.1.2 pyOMA2

pyOMA2 is an opensouce toolbox that include serval OMA techniques [26]. In this thesis only the SSI-cov are used as explained before and the theory alings with Section 6.1.1, there is the possibility for both and single and multiple setup, which simply means if the data is made from a single experiment or from multiple. In this thesis the single setup are used. The process can be shown in a simplified way by:

- 1. Setup: Wrap the raw timeseries and its sampling frequency in a container that can apply optional preprocessing (filtering, detrending, decimation).
- 2. Run: Execute one or more algorithms that read the clean data and write their results (poles, mode shapes, spectra) back into the container.
- 3. *Inspect:* View stabilisation diagrams, pole tables and modeshape animations through interactive plotting helpers or export them for postprocessing.

For the SSIcov algorithm, there are several user chosen parameters. The four most important are the number of block rows and the model order (for which both minimum and maximum values can be specified), as well as the soft and hard stability thresholds. The block rows and model order are selected based on the system characteristics, and the threshold in Equation (6.5) can serve as a guideline. The soft criteria determine whether a pole is considered stable, the default pyOMA thresholds are as follows for the natural frequency f_n , the damping ratio ζ_n , and the Modal Assurance Criterion (MAC) values of the mode shapes:

$$\frac{|f_n(k) - f_n(k+1)|}{f_n(k)} < 0.01, (6.23)$$

$$\frac{|\zeta_n(k) - \zeta_n(k+1)|}{\zeta_n(k)} < 0.05, \tag{6.24}$$

$$1 - \text{MAC}(\phi_n(k), \phi_n(k+1)) < 0.02. \tag{6.25}$$

A pole $\lambda(k)$ is considered stable if all the soft criteria are met for both $\lambda(k)$ and the subsequent pole $\lambda(k+1)$. The hard thresholds, on the other hand, remove poles from the system, for example, the default damping ratio threshold is $\zeta = 0.1$, meaning any pole with a damping ratio exceeding 10% is discarded. There are also limits on modal phase collinearity and the maximum coefficient of variation, but these will not be covered here.

MAC quantifies the similarity between two mode shape vectors and takes values in [0,1] (1 means identical up to scaling, 0 means orthogonal). It is computed as:



$$MAC(\phi_1, \phi_2) = \frac{|\phi_1^H \phi_2|^2}{(\phi_1^H \phi_1)(\phi_2^H \phi_2)},$$
(6.26)

here, ϕ_1,ϕ_2 are mode shape vectors and $(\cdot)^H$ denotes the Hermitian (conjugate) transpose. MAC is used above only as a stability check within the SSI-cov identification. It will not be included in the subsequent model updating procedure.

6.1.3 Data results LACFLEX

With the simulation from LACFLEX, the modal parameters of the jacket OWT can be estimated using SSI-cov. As mentioned in Section 5.3, the data record spans only ten minutes with a sampling frequency of 100 Hz. Having such short records can be challenging for accurately estimating the modal parameters. Furthermore the SSI-cov performs significantly better with larger data sets. This improvement arises because the algorithm's core relies on constructing covariance matrices from the time series data. Longer data records lead to more statistically robust estimates of these covariances, which in turn produces a more accurate system model. More data improves the signal-to-noise ratio, allowing the algorithm to better distinguish the true structural response from random noise [27]. In Figure 6.1 the stabilization diagram for the frequency across model order is shown.

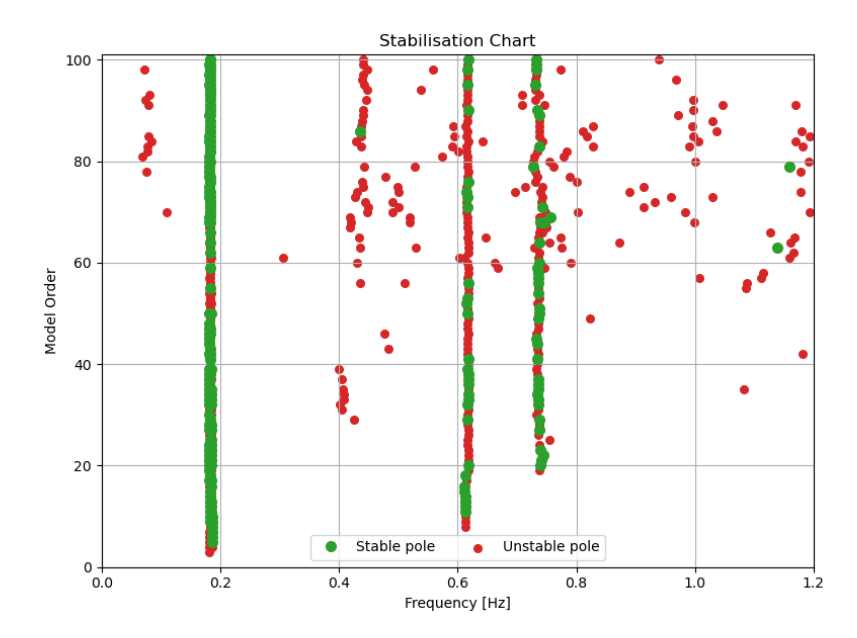


Figure 6.1: Stabilization diagram for frequency across model order.

Figure 6.1 shows four stabilizing poles: two near 0.2 Hz, corresponding to the first bending modes in the x and y directions, one just above 0.6 Hz, likely representing a torsional mode, and another around 0.75 Hz, which is likely the second bending mode. A detailed view of the two poles at 0.2 Hz is provided in Appendix 11.2.

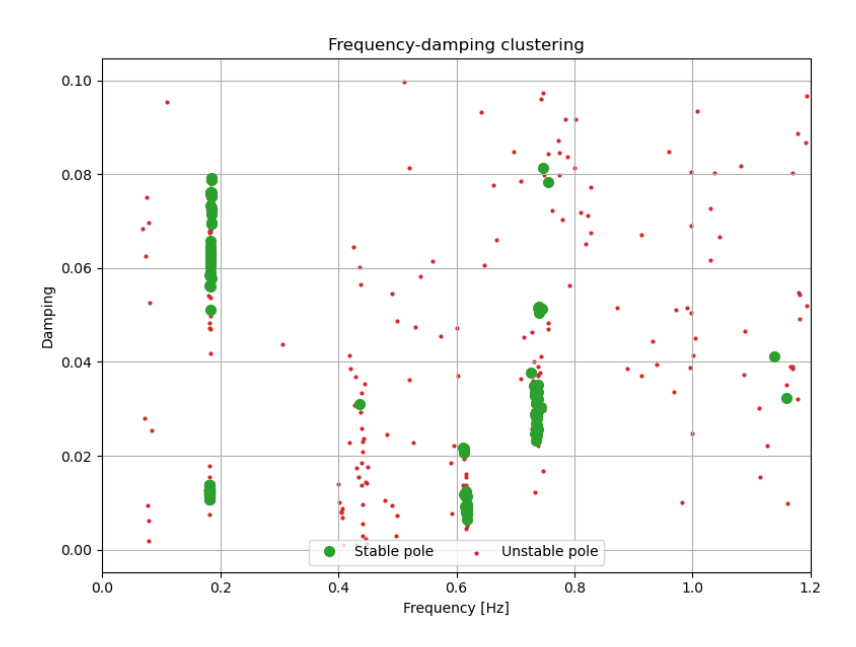


Figure 6.2: Stabilization diagram for damping ratio as function of frequency.

From the SSI-cov stabilization diagram, it was decided to consider only the first two bending modes. The mode around 0.6 Hz (mode 3) exhibited a higher frequency than mode 3 in the calibrated FE Python model, since the other modes were lower, they were excluded from the subsequent model update. While the frequencies stabilize across model order, the damping estimates remain quite scattered. Damping is known to be more difficult to estimate, and with only ten minutes of data, a perfectly tight cluster is not expected. The damping ratios for mode 1 form a closely spaced cluster, whereas those for modes 2 and 4 are more dispersed. Mode 2's damping is much higher than mode 1's, possibly due to blade pitch damping, but a damping ratio of 6-8% is unexpectedly large. Consequently, only the frequencies of modes 1, 2, and 4 and the damping ratio of mode 1 are used for the model update. The selected parameters for model order 35 are shown in Table 6.1.

Table 6.1: Final model parameters for the system.

	Mode 1	Mode 2	Mode 4
Fn [Hz]	0.1819	0.1838	0.7362
ζ [-]	0.0127	$0.0590^{\rm a}$	$0.0281^{\rm a}$

^a Reported for completeness, not used in the model-updating.

The values estimated from the OMA based on the LACFELX simulation are slightly lower than those from the FE software ROSAP and the Python based FE model however, these will now be considered the true values for the system. Given that the values are lower, the implementation of the viscoelastic model should be able to estimate them to some extent. If the values were higher, the FE model would encounter problems, since the highest possible natural frequency occurs when the support model is equivalent to a simple support, as shown in Table 5.4.



7 Digital twins - in house Python

Digital twins are computer models that mirror physical assets in real-time, continuously updating themselves using data from sensors and other monitoring sources on the actual structure. For structural and geotechnical systems, the digital twin typically consists of a Finite Element (FE) model that captures the system's stiffness, mass, and damping properties, while the live data stream includes measured operational responses such as accelerations, strains, or displacements.

In this thesis, the physical asset is represented by an offshore foundation supported on piles, modeled using the FE software ROSAP. Since no actual physical structure is involved in this study, the updating process consists of FE-to-FE model updating, where the ROSAP model serves as the reference "physical asset". An in-house Python code is employed to: (a) build a full-order FE model, and (b) incorporate viscoelastic soil damping by attaching Zener or Kelvin-Voigt models to the support Degrees Of Freedom (DOF). An illustration of this approach is shown in Figure 7.1.

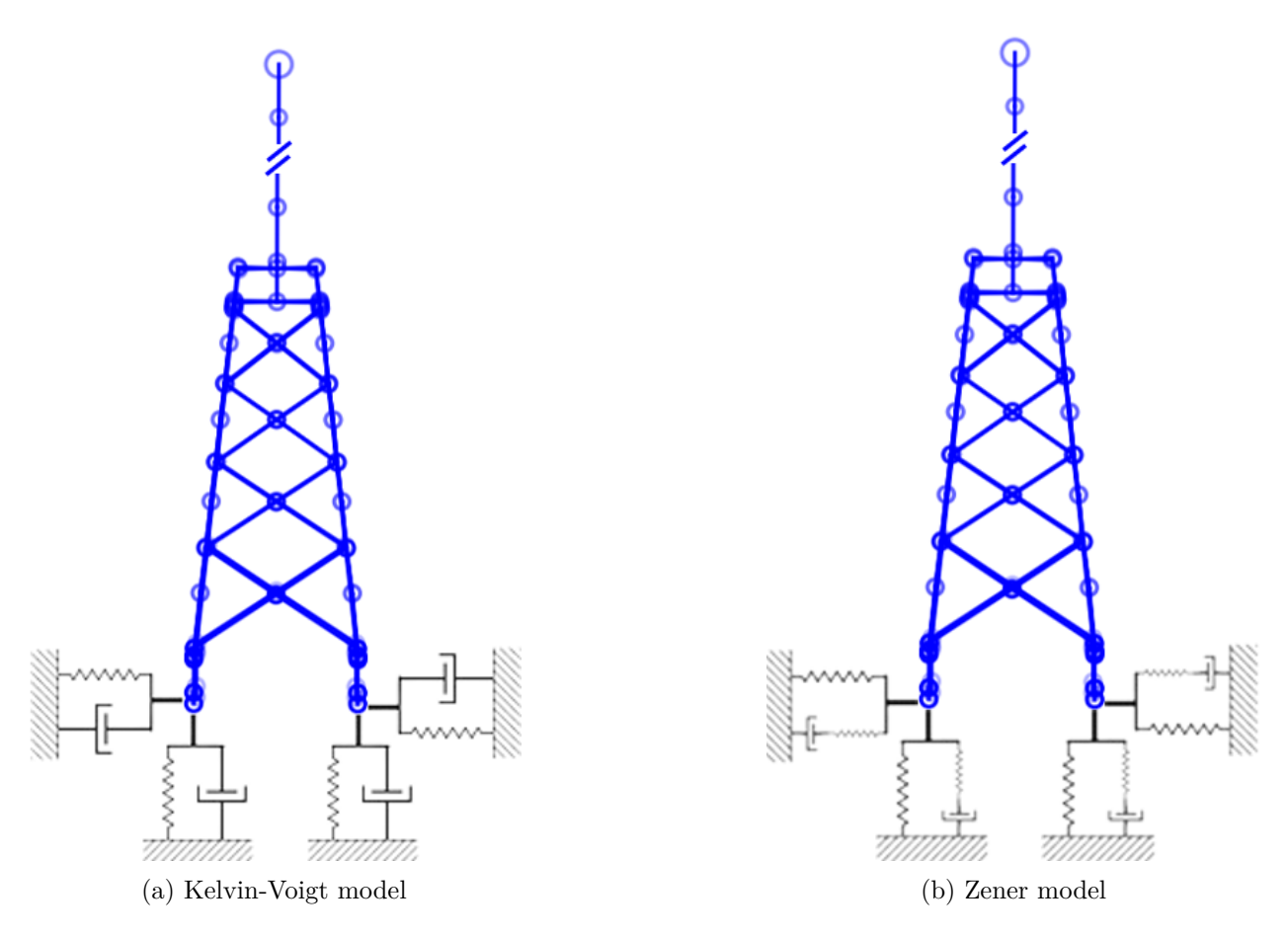


Figure 7.1: The jacket OWT with the viscoelastic model as support, where (a) has a Kelvin Voigt model and (b) has a Zener model.

7.1 Kelvin-Voigt implementation

To incorporate the Kelvin-Voigt model into the FE model, the stiffness (k) and damping coefficient (c) are added to the global matrices at the corresponding translational support DOF. Where:

- n be the number of global structural DOFs.
- n_s the number of support DOFs that carry an the Kelvin-Voigt model.
- $\mathbf{R}^{\mathbf{n}_s \times \mathbf{n}}$ a Boolean mapping matrix that extracts those support DOFs from the global vector.

The augmented state vector is:

$$\mathbf{x} = \begin{bmatrix} \mathbf{x} & \dot{\mathbf{x}} \end{bmatrix}^T, \tag{7.1}$$

which yields the first-order system:

$$\frac{d}{dt} \underbrace{\begin{bmatrix} \mathbf{x} \\ \dot{\mathbf{x}} \end{bmatrix}}_{\mathbf{X}} = \underbrace{\begin{bmatrix} \mathbf{0} & \mathbf{I} \\ -\mathbf{M}^{-1} (\mathbf{K} + \mathbf{R}^{\mathsf{T}} \mathbf{K}_0 \mathbf{R}) & -\mathbf{M}^{-1} (\mathbf{C} + \mathbf{R}^{\mathsf{T}} \mathbf{C}_0 \mathbf{R}) \end{bmatrix}}_{\mathbf{A}} \mathbf{x} + \underbrace{\begin{bmatrix} \mathbf{0} \\ \mathbf{M}^{-1} \end{bmatrix}}_{\mathbf{B}} \mathbf{f}_{\text{ext}}(t). \tag{7.2}$$

Using the FE mass matrix (\mathbf{M}) , stiffness matrix (\mathbf{K}) and Rayleigh damping matrix (\mathbf{C}) described in Chapter 3, together with

$$\mathbf{K}_0 = \operatorname{diag}(k_0(1), \dots, k_0(n_s)), \mathbf{C}_0 = \operatorname{diag}(c_0(1), \dots, c_0(n_s)). \tag{7.3}$$

The resulting jacket OWT model incorporates Kelvin-Voigt support conditions.

7.2 Zener implementation

To incorporate the Zener model into the FE formulation, the initial stiffness (k_0) is assembled directly into the global stiffness matrix, while the additional stiffness (k_1) and the dashpot coefficient c enter through one extra internal variable per support DOF, as in the single DOF Zener element (Section 4.4). As in the Kelvin-Voigt implementation (Section 7.1), let n be the total number of structural DOFs, let n_s denote the number of support DOFs carrying a standard linear solid, and introduce the Boolean extraction matrix $\mathbf{R} \in \{0,1\}^{n_s \times n}$ that selects those support DOFs from the global vectors.

The augmented state vector is:

$$\mathbf{x} = [\mathbf{x} \quad \dot{\mathbf{x}} \quad \mathbf{z}]^T, \tag{7.4}$$

which yields the first-order system:



$$\frac{d}{dt} \underbrace{\begin{bmatrix} \mathbf{x} \\ \dot{\mathbf{x}} \\ \mathbf{z} \end{bmatrix}}_{\mathbf{X}} = \underbrace{\begin{bmatrix} \mathbf{0} & \mathbf{I} & \mathbf{0} \\ -\mathbf{M}^{-1} (\mathbf{K} + \mathbf{R}^{\mathsf{T}} \mathbf{K}_{0} \mathbf{R}) & -\mathbf{M}^{-1} \mathbf{C} & -\mathbf{M}^{-1} \mathbf{R}^{\mathsf{T}} \\ \mathbf{0} & \mathbf{K}_{1} \mathbf{R} & -\mathbf{\Lambda} \end{bmatrix}}_{\mathbf{A}} \mathbf{x} + \underbrace{\begin{bmatrix} \mathbf{0} \\ \mathbf{M}^{-1} \\ \mathbf{0} \end{bmatrix}}_{\mathbf{B}} \mathbf{f}_{\text{ext}}(t). \tag{7.5}$$

Using the FE mass matrices, as before in Section 7.1, together with

$$\mathbf{K}_{0} = \operatorname{diag}(k_{0}(1), \dots, k_{0}(n_{s})), \, \mathbf{K}_{1} = \operatorname{diag}(k_{1}(1), \dots, k_{1}(n_{s})), \, \mathbf{\Lambda} = \operatorname{diag}(\frac{k_{1}(1)}{c(1)}, \dots, \frac{k_{1}(n_{s})}{c(n_{s})}).$$
(7.6)

The resulting jacket OWT model incorporates Zener support conditions. The Maxwell branch for each translational support DOF is included in the same way as in Section 4.4, introducing one additional state variable per support DOF in matrix form.

8 Model updating

Model updating is a fundamental process in digital twin technology where computational models are calibrated against experimental or operational data to improve their predictive accuracy. This process involves adjusting uncertain model parameters to minimize the discrepancy between predicted and observed system responses. The optimization problem is typically formulated minimization, where the objective function represents the weighted sum of squared residuals between model predictions and measurements.

The identification of the parameters in the Kelvin-Voigt and Zener models requires solving an optimization problem to determine the optimal values of (k) and (c) for the Kelvin-Voigt model, and (k_0) , (c), and (k_1) for the Zener model, that best fit the OMA modal parameters. Parameter estimation is formulated as a minimization problem in which the objective function quantifies the discrepancy between model predictions and experimental observations. The general model updating problem can be expressed as:

$$\boldsymbol{\theta}^* = \arg\min_{\boldsymbol{\theta}} J(\boldsymbol{\theta}), \tag{8.1}$$

where θ represents the vector of uncertain parameters to be updated, $J(\theta)$ is the objective function quantifying the model data mismatch, and θ^* denotes the vector of updated parameters. The parameters to be updated here are those in the two models:

$$\boldsymbol{\theta}_{kv} = [k, c], \tag{8.2}$$

$$\boldsymbol{\theta}_z = [k_0, c, k_1], \tag{8.3}$$

where θ_{kv} denotes the parameter vector to be updated for the KelvinVoigt model, and θ_z denotes the parameter vector to be updated for the Zener model. It should be noted that the damping matrix \mathbf{C} is included in the FE formulation and provides 1% damping for the first mode as stated before in Section 4.1, the damping generated by the viscoelastic model should account for the difference between the damping estimated from OMA and the Rayleigh damping.

8.1 Cost function formulation

The cost function is designed to minimise the discrepancy between the model-predicted dynamic characteristics and the experimental measurements. In this study, only the natural-frequency residuals of modes 1, 2, and 4, and the damping-ratio residual of mode 1, are included see Section 6.1.3. Accordingly, the cost function is expressed as:

$$J(\boldsymbol{\theta}) = \sum_{i=1}^{3} w_{\omega} \left(\frac{\omega_{\text{OMA},i} - \omega_{\text{FE},i}}{\omega_{\text{OMA},i}} \right)^{2} + w_{\zeta} \left(\frac{\zeta_{\text{OMA}} - \zeta_{\text{FE}}}{\zeta_{\text{OMA}}} \right)^{2}, \tag{8.4}$$



here, $\omega_{\rm OMA}$ and $\omega_{\rm model}$ denote the natural frequencies measured experimentally with OMA and predicted by the FE model, respectively, while $\zeta_{\rm OMA}$ and $\zeta_{\rm FE}$ are the corresponding damping ratios.

The weighting factors w_{ω} and w_{ζ} scale the frequency and damping residuals to reflect measurement uncertainty or the relative importance of each quantity in the optimisation. In this thesis, each residual is normalised by its experimental value so that the frequency and damping terms contribute equally to the total cost. With this normalisation, the weighting factors are simply set to unity, i.e. $w_{\omega} = w_{\zeta} = 1$.

The model parameters ω, ζ are obtained from the FE model described earlier in Equation (7.2) and (7.5), with the viscoelastic models as the support condition. They are computed by a Python function ModelPAR, which solves the eigenvalue problem of the state-space matrix **A**, with the current updating parameters as inputs, this process is expressed as:

$$[\omega, \zeta] = \text{ModelPAR}(\boldsymbol{\theta}). \tag{8.5}$$

Selecting the correct modal frequencies is crucial. Adding a Zener element at the support introduces purely real modes at 0 Hz and can generate additional low-frequency spurious modes. These modes must be filtered out so that only the relevant modes are compared. Otherwise, the cost function can become artificially large and disrupt the updating algorithm.

8.2 Nelder-Mead optimization

The minimization problem in this thesis is solved with the Nelder-Mead algorithm from the python library SciPy [28]. Nelder-Mead is a derivative free method for minimizing a function of a small number of variables. It maintains a simplex a set of n+1 points (a triangle in 2D, tetrahedron in 3D, etc.). The simplex is repeatedly reshaped to find lower function values, the method can be divided into the following steps:

- 1. Order the simplex points by their objective values (best to worst).
- 2. Centroid: Compute the average of all points except the worst.
- 3. Reflect the worst point through the centroid to test for improvement.
- 4. Expand further in that direction if the reflected point is exceptionally good, otherwise contract back toward the centroid.
- 5. If neither step helps, shrink the entire simplex toward the best point and iterate.

Because it relies solely on function evaluations not gradients Nelder-Mead excels on low-dimensional, noisy, or blackbox problems where derivatives are unavailable or unreliable, though it scales poorly to high dimensions and offers no guarantee of finding the global minimum.



Parameter bounds are enforced to ensure physical meaningfulness and help the algorithm search in area, the bound used for the Kelvin-Voigt model updating was:

$$k \in [10^7, 10^{14}],$$
 (8.6)

$$c \in [10^4, 10^{14}]. \tag{8.7}$$

For the Zener model the Parameter bounds was:

$$k_0 \in [10^7, 10^{14}],$$
 (8.8)

$$c \in [10^4, 10^{14}], \tag{8.9}$$

$$k_1 \in [10^7, 10^{14}].$$
 (8.10)

The optimization process benefits from careful initial guess, often using multiple starting points to avoid convergence to local minima. The wide parameter ranges, particularly for η spanning several orders of magnitude.

8.3 Verification of the Zener model

To verify the implementation of the Zener model with additional internal variables, the system response was examined for fixed stiffnesses k_1 and k_2 while the damping coefficient c was varied. Two limiting cases are expected:

- $c \to 0$: the damper disconnects k_2 , so the system behaves as if only k_1 is present.
- $c \to \infty$: the damper acts as a rigid link, placing k_2 in parallel with k_1 , the effective stiffness becomes $k_{\text{eff}} = k_1 + k_2$.

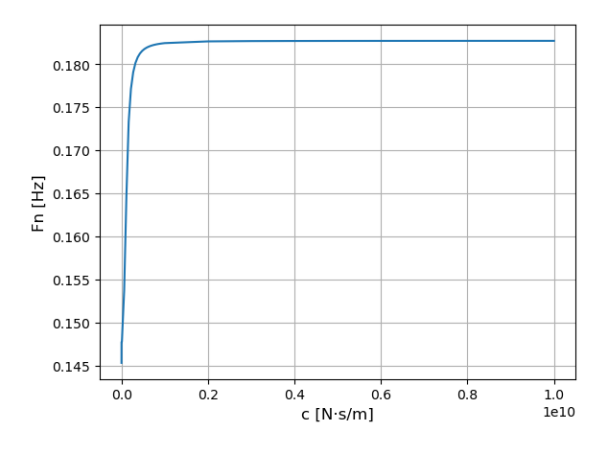


Figure 8.1: Natural frequency versus damping coefficient (c) for the Zener model with constant (k_1) and (k_2) .

The curve in Figure 8.1 starts at approximately 0.145 Hz when c = 0 and rises toward 0.183 Hz as c becomes very large. These endpoints match the natural frequencies of the reference systems that contain only k_1 or $k_1 + k_2$, respectively, confirming that the Zener model is implemented correctly.



8.4 Results

Below, the optimization results for the minimization problem are presented for the jacket offshore wind turbine using the two support condition variants, the Kelvin-Voigt model and the Zener model.

8.4.1 Kelvin-Voigt model

To start the modelupdating scheme, the Kelvin-Voigt model is used, minimizing the cost function in Equation (8.4) with the Nelder-Mead algorithm. A few different starting points were used for the algorithm to find the best point, as the algorithm does not converge to the same optimal value every time. These different optimal points are then plotted on a surface plot of the cost function to better visualise the problem. The surface plot in Figure 8.2 shows three different points, which are the optimal values found by the algorithm.

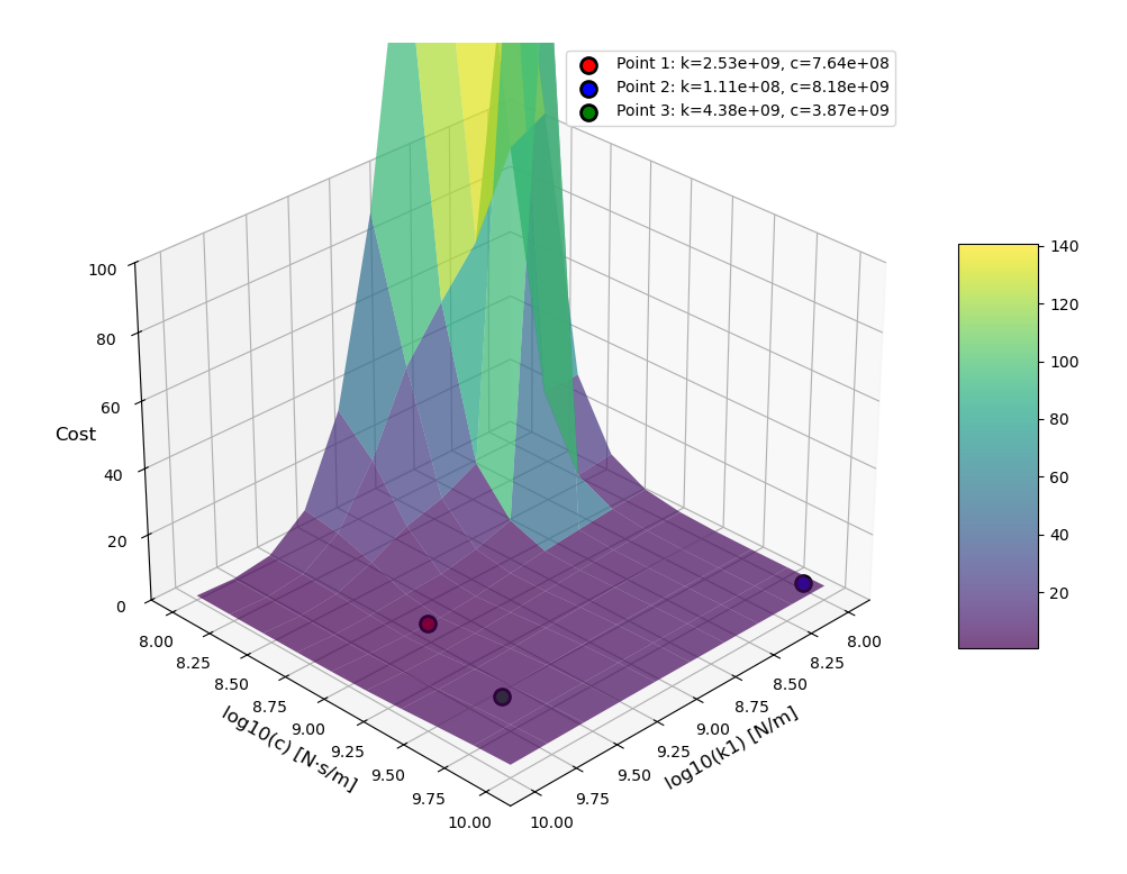


Figure 8.2: Surface plot of the cost function for the Kelvin-Voigt model, showing three different optimal values obtained from distinct initial guesses.

Point 1 from Figure 8.2, with a stiffness of $k=2.5\times 10^9\,\frac{\rm N}{\rm m}$ and a damping coefficient of $c=7.6\times 10^8\,\frac{\rm N\cdot s}{\rm m}$, yielded the lowest cost among the three candidate solutions and among the other optima found by the algorithm. To verify that this point is at least a local minimum, a close up of the cost function is shown in Figure 8.3. Model updating with the Nelder-Mead algorithm does not guarantee a global optimum, but it is considered sufficient for the present purpose.

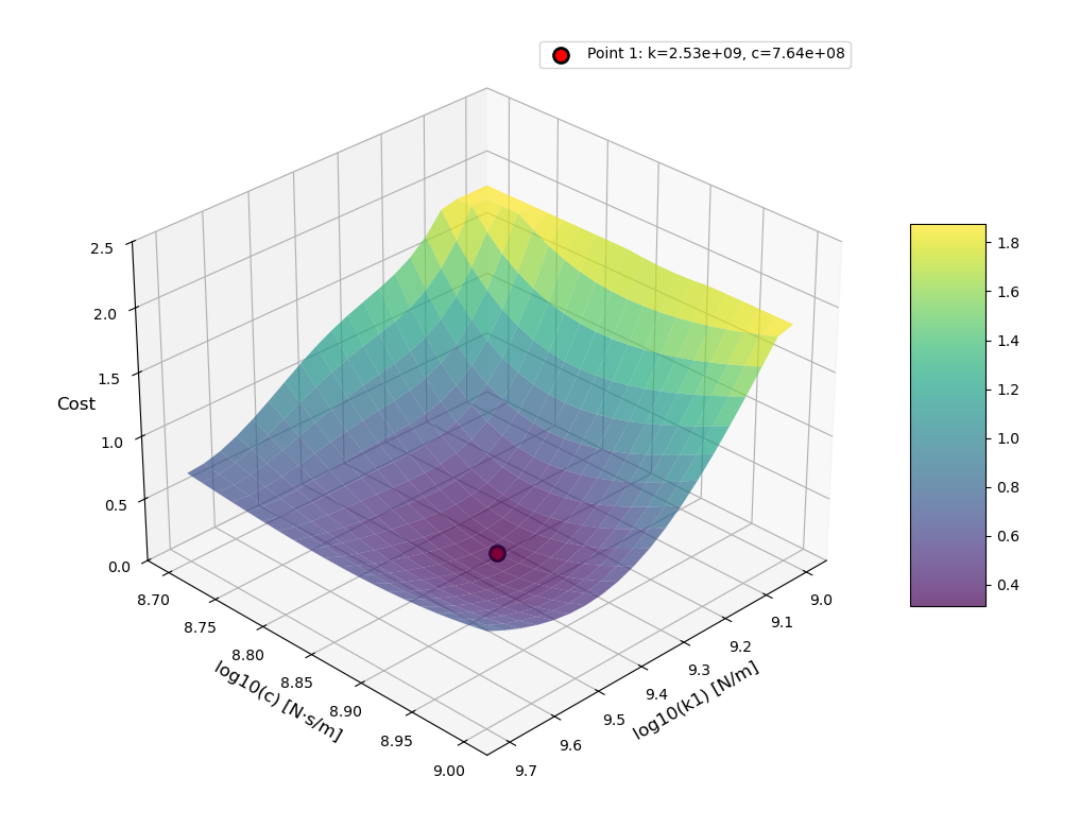


Figure 8.3: Surface plot of the cost function for the Kelvin-Voigt model, with a close up of point 1 from Figure 8.2.

The results of the optimal modal parameters for point 1 with the final natural frequency and damping ratio can be seen in Tables 8.1 and 8.2.

Table 8.1: Comparison of optimized point 1 and experimental natural frequency for Kelvin-Voigt model.

	Mode 1	Mode 2	Mode 4
Optimized	0.1812	0.1845	0.7362
Experimental	0.1819	0.1838	0.7362
Relative Error (%)	0.401	0.384	0.002

Table 8.2: Comparison of optimized point 1 and experimental damping for mode 1 and 2 for the Kelvin-Voigt model.

	Mode 1	Mode 4
Optimized	0.01277	0.04237
Experimental	0.01269	0.02806
Relative Error (%)	0.668	50.49

From the results of the updating algorithm, it can be seen that the Kelvin-Voigt model can catch both the natural frequency of the system for modes 1, 2, and 4 with a relative error of less than 1% and the damping for the first mode with a relative error of 0.7%. The damping for mode 4 was not included in the updating scheme but shown here to Illustrate what damping the Kelvin-Voigt model will produce for mode 4, and ended up with an 50% relative error.

To investigate how the complex eigenvalues change as the damping coefficient c varies, a rootlocus plot is generated using the stiffness values from point 1 and 2 while sweeping c from 0 to ∞ , thereby revealing two limiting cases: when c = 0, only the spring element of the Kelvin-Voigt model remains active, whereas when $c = \infty$, the damper rigidly restrains the three translational support degrees of freedom, so the support behaves as a simple support.

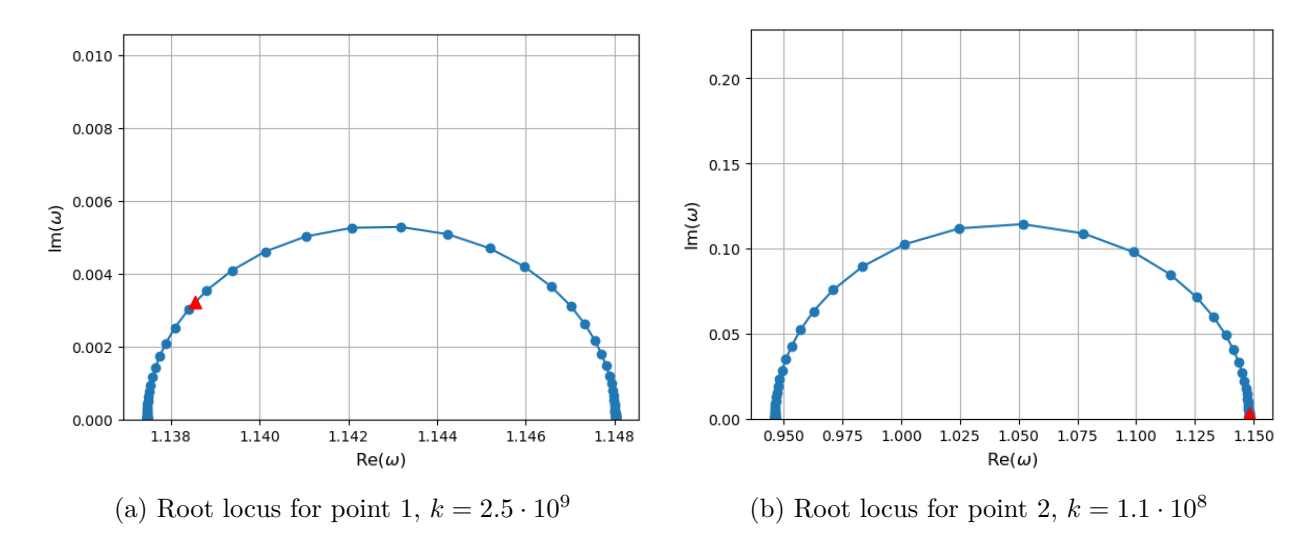


Figure 8.4: Root locus plots for the Kelvin-Voigt models mode 1 of the optimized systems, where (a) uses the stiffness (k) from point 1, and (b) uses the stiffness (k) from point 2. The red triangle represents the optimal point. Note that only the Kelvin-Voigt damping is included. The global Rayleigh damping matrix is set to 0.

The rootlocus plot shows that, for point 1, the limiting cases at c=0 and $c=\infty$ are close to each other, and the optimal point lies at the beginning of the curve. This indicates that increasing the damping parameter c raises the natural frequency slightly but does not fundamentally change it from the natural frequency of the undamped eigenvalue problem, which corresponds to the limiting case c=0. By contrast, the root-locus plot for the stiffness from point 2 exhibits a much larger separation between the two limiting cases. The algorithm therefore chooses to nearly lock the damper $(c \to \infty)$ to increase the natural frequency, but this choice fundamentally alters the natural frequency relative to the undamped eigenvalue problem. Table 8.3 lists the natural frequencies of the optimal modes obtained with the parameters from point 2 for both the complex eigenvalue and undamped eigenvalue problems.

Table 8.3: Comparison of the undamped natural frequency and the natural frequency obtained from the complex eigenvalues of the Kelvin-Voigt model.

	Mode 1	Mode 2	Mode 4
damped	0.1827	0.1861	0.7478
undamped	0.1506	0.1522	0.477
Relative Error (%)	21.3	22.3	56.8

Table 8.3 shows that increasing the damping coefficient c fundamentally alters the undamped natural frequency. This effect must be considered when updating the model to ensure that it performs correctly in both dynamic analyses and static analyses in which damping is not included.

8.4.2 Zener model

The Zener model suffers from the same issue as the Kelvin-Voigt model, the algorithm produces different results depending on the initial values, since the cost function has multiple local minima. The optimal values cannot be plotted in the same figure as in Figure 8.2, because the problem is now four dimensional rather than three dimensional. Two of the best points are shown in Table 8.4.

Table 8.4: Comparison of the two optimal point for the Zener model.

	$\mathbf{k}_0[\mathrm{N/m}]$	$\mathbf{c}[\mathrm{Ns/m}]$	$\mathbf{k}_1[\mathrm{N/m}]$
Point 1	4.4×10^{9}	3.76×10^{9}	6.14×10^{12}
Point 2	2.62×10^{9}	8.65×10^{8}	9.99×10^{9}

From Table 8.4, it is clear that the two points differ significantly. The primary reason for including both is that, at point 1, the algorithm actually tries to reduce the Zener model to the Kelvin-Voigt model. The values for the natural frequency and damping for point 1 are shown in Table 8.5 and 8.6, respectively.



Table 8.5: Comparison of optimized point 1 and experimental natural frequencies for the Zener model.

	Mode 1	Mode 2	Mode 4
Optimized	0.1817	0.1851	0.7296
Experimental	0.1819	0.1838	0.7362
Relative Error (%)	0.102	0.698	0.894

Table 8.6: Comparison of optimized point 1 and experimental damping for mode 1 and 2 for the Zener model.

	Mode 1	Mode 4
Optimized	0.01266	0.02764
Experimental	0.01269	0.02806
Relative Error (%)	0.159	1.475

Analysis of the updating algorithm results in Table 8.5 and 8.6 for point 1 shows that the Zener model predicts the systems natural frequencies for modes 1, 2, and 4 with relative errors below 1%, and estimates the damping of mode 1 with a relative error of 0.2%. Although mode 4's damping was not included in the original updating scheme, it is reported here to illustrate the Zener models performance it predicts mode 4's damping with a relative error of 1.5%, which still represents very good agreement. As mentioned before, this point was included because the algorithm selected k_1 , causing the support to behave as a Kelvin-Voigt model. In Figure 8.5, a sensitivity analysis at point 1 was performed by varying each model parameter $(k_0, c, and k_1)$ by $\pm 50\%$, while holding the other two parameters constant at their optimal values.

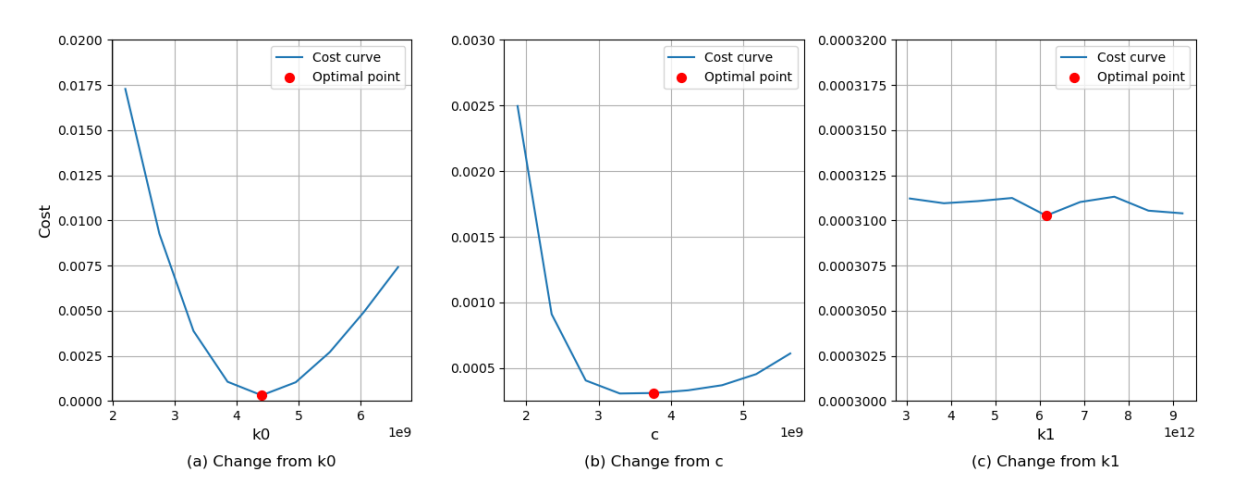


Figure 8.5: Sensitivity analysis at point 1 showing the effect of $\pm 50\%$ changes in (a) base stiffness (k_0) , (b) damping coefficient (c), and (c) secondary stiffness (k_1) , with all other parameters held constant.

As shown in Figure 8.5, the local minimum is clearly identified. Figures 8.5 (a) and (b) exhibit a distinct minimum when the parameters are varied by $\pm 50\%$, whereas Figure 8.5 (c) remains nearly constant for k_1 , likely due to numerical error since k_1 is set so large that the model effectively reduces to a Kelvin-Voigt model.

At point 2, the optimized parameters correspond to a Zener model. The resulting natural frequencies and damping ratios at point 2 are listed in Table 8.7 and 8.8, respectively.

Table 8.7: Comparison of optimized point 2 and experimental natural frequency for the Zener model.

	Mode 1	Mode 2	Mode 4
Optimized	0.1813	0.1847	0.7358
Experimental	0.1819	0.1838	0.7362
Relative Error (%)	0.338	0.452	0.048

Table 8.8: Comparison of optimized point 2 and experimental damping for mode 1 and 4 for the Zener model.

	Mode 1	Mode 4
Optimized	0.01269	0.03474
Experimental	0.01269	0.02806
Relative Error (%)	0.001	23.77

Analysis of the updating algorithm results at point 2 Table 8.7 and 8.8 show that the Zener model predicts the natural frequencies of modes 1, 2, and 4 with relative errors below 0.5%, and estimates the damping ratio of mode 1 with a relative error of 0.001%. The damping ratio of mode 4, which was not included in the updating scheme, exhibits a relative error of 24%. Overall, the Zener model improves the estimates for all parameters except the natural frequency of mode 1 and the damping of mode 4. As with point 1, a sensitivity analysis was performed at point 2 and is shown in Figure 8.6. Each model parameter $(k_0, c, and k_1)$ was varied by $\pm 50\%$, and all three subplots in Figure 8.6 (a)-(c) illustrate a clear minimum at point 2.

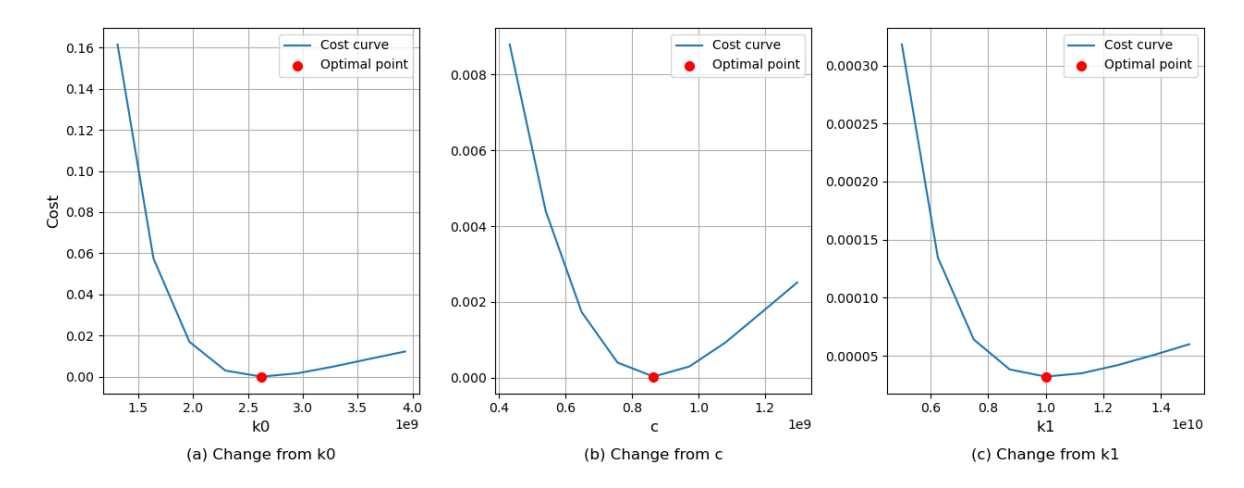


Figure 8.6: Sensitivity analysis at point 2 showing the effect of $\pm 50\%$ changes in (a) base stiffness (k_0) , (b) damping coefficient (c), and (c) secondary stiffness (k_1) , with all other parameters held constant.

To investigate the complex eigenvalues of the Zener model, root locus plots for points 1 and 2 are presented in Figure 8.7.

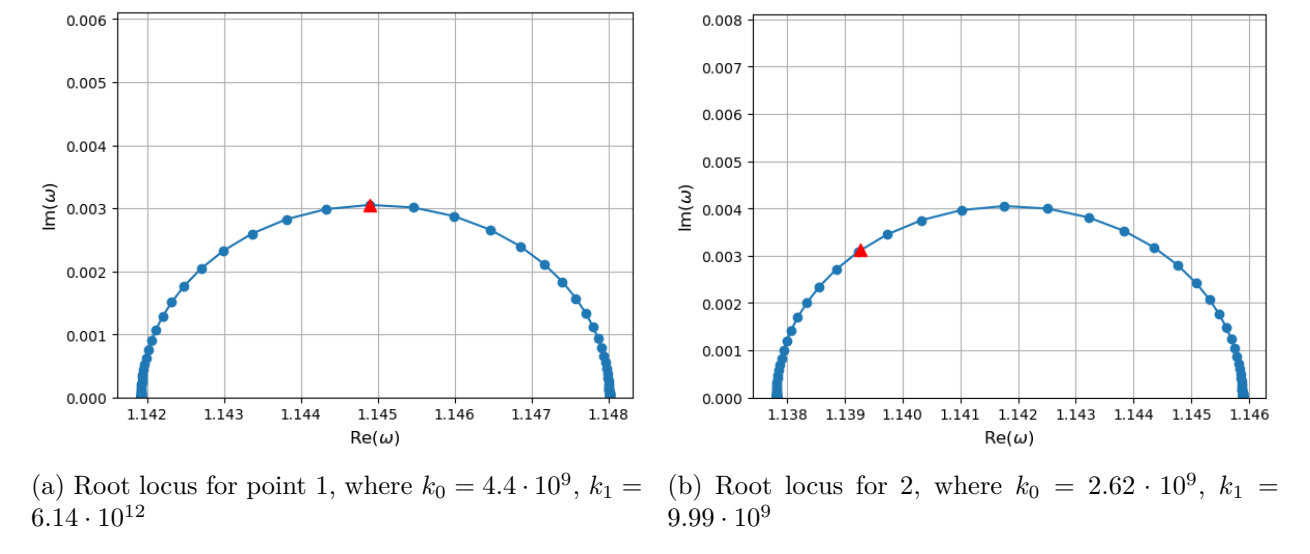


Figure 8.7: Root locus plots for the Zener models mode 1 of the optimized systems, where (a) uses the stiffness (k_0) and (k_1) from point 1, and (b) uses the stiffness (k_0) and (k_1) from point 2. The red triangle represents the optimal point. Note that only damping from the Zener model is included. The global Rayleigh damping matrix is set to 0.

From the root locus plot of the Zener model, it is shown that the algorithm chooses k_0 so the limiting case of c=0 is close to the values from OMA, and then adjusts with k_1 and c to match the damping ratio. The Zener model has a bit more flexibility when it comes to changing the complex eigenvalues, as it can also move the limiting case of $c \to \infty$ down by adjusting k_1 and k_2 .



9 Conclusion

The objective of this thesis was to investigate whether soil damping could be incorporated into a simple digital twin (DT) via a viscoelastic support model capable of capturing both the structure's natural frequencies and damping. The research was structured around three main objectives, and the following conclusions can be drawn:

(i) Simulation of structural response data using ROSAP and LACFLEX:

Simulations were successfully carried out using ROSAP and LACFLEX to generate structural response data, and the viscoelastic Kelvin-Voigt model was included along the piles to incorporate damping from the soil-pile interaction, with stiffness derived from the p-y springs and equivalent damping coefficient. The simulations made in LACFLEX can then be used for further analysis using Operational Modal Analysis OMA.

(ii) Application of OMA to identify modal parameters and soil damping characteristics:

OMA using the Stochastic Subspace Identification Covariance-driven (SSI-cov) algorithm was successfully applied to the simulated time series data. The OMA approach reliably identified the structure's natural frequencies and provided estimates of modal damping ratios. However, damping is inherently more challenging to estimate than natural frequencies due to its sensitivity to measurement noise, environmental conditions, and modeling uncertainties. This difficulty was compounded in the wind turbine system by complex aerodynamic interactions that caused damping estimates to vary significantly across modes, for example, mode 2 exhibited approximately 6% damping while mode 1 showed only 1.3%. Since modes 1 and 2 are practically the same mode, and modifying the damping in the support structure alone cannot simultaneously achieve accurate damping values for both, it was concluded that the model updating should focus on the natural frequencies of modes 1, 2, and 4, while updating the damping only for mode 1.

(iii) Development of a simplified 3D DT with viscoelastic soil models:

A simplified Finite Element (FE) model incorporating viscoelastic support conditions was successfully developed in Python. The modal updating scheme accurately matched three selected natural frequencies and the first damping ratio, achieving relative errors below 1% compared to OMA results for both Kelvin-Voigt and Zener models. However, the updating procedure must ensure physically realistic viscoelastic parameters to avoid unrealistic stiffness values that could adversely affect static analyses. The optimization involves multiple local minima, necessitating careful selection of initial conditions and multiple starting points when using the Nelder-Mead algorithm.

Overall, it can be concluded that a simple FE model can successfully incorporate viscoelastic support conditions and, through appropriate parameter selection, accurately reproduce both natural frequencies and damping characteristics identified through OMA.



10 Future work

From this thesis, several promising future research objectives emerge that could advance this field of study.

Instead of setting the damping ratio using the minimum value for the first natural frequency, future research could investigate using both the ω_{\min} and the damping coefficient c in the viscoelastic model as updating parameters to capture the damping ratio for multiple modes while maintaining the simplicity of the Kelvin-Voigt or Zener model. By also adjusting the ω_{\min} in the Rayleigh damping matrix in the Finite Element (FE) model, there is potential for the updating scheme to capture damping ratios for multiple modes with improved accuracy.

To advance the estimation and updating of damping using viscoelastic models, implementing a Prony model (generalized Maxwell model) for the support conditions could be particularly valuable for capturing the damping ratios of multiple modes more accurately. The Prony model is similar to the Zener model but incorporates multiple Maxwell branches instead of just one, potentially allowing the damping ratios of different modes to be estimated using a larger combination of Maxwell branches while maintaining the initial stiffness from the parallel branch containing only stiffness. Calibrating a Prony model will introduce more variables into the support model, therefore, additional parameters such as extra natural frequencies, damping ratios or mode shapes should be included in the updating scheme. Because the number of unknowns increases, regularization could be applied to ensure stable convergence, good optimal solutions and physically meaningful results.

Since all the digital twins in this study were developed using FE-to-FE models, an interesting future project would be to utilize actual real-world data from a jacket offshore wind turbine and investigate whether modeling soil damping using viscoelastic models can capture the real behavior of soil-pile interaction. This could potentially be enhanced through the implementation of a Prony model or generalized Maxwell model to capture damping across multiple modes with greater fidelity.

Using viscoelastic models such as the Zener model introduces an additional purely real pole associated with the relaxation of the viscoelastic elements. An interesting direction for future research would be to estimate these real poles and incorporate them into the model updating process. This could be achieved either by adding an extra Maxwell branch variable as done for the Zener model into FE simulations (e.g., ROSAP and LACFELX used in this thesis) or by extracting these poles from real world data.



References

- [1] Abdollah Malekjafarian et al. "Foundation damping for monopile supported offshore wind turbines: A review". In: *Marine Structures* 77 (May 2021). DOI: 10.1016/j.marstruc.2021.102937. URL: https://www.sciencedirect.com/science/article/pii/S0951833921000058.
- [2] OpenFAST Team. SubDyn modelling considerations: damping options and implementation. https://openfast.readthedocs.io/. (visited on 01/03/2025).
- [3] Aemilius A. W. van Vondelen et al. "Damping Identification of Offshore Wind Turbines Using Operational Modal Analysis: A Review". In: Wind Energy Science 7.1 (2022), pp. 161–184. DOI: 10.5194/wes-7-161-2022. URL: https://doi.org/10.5194/wes-7-161-2022.
- [4] C. Chen and P. Duffour. "Modelling damping sources in monopile-supported offshore wind turbines". In: Wind Energy 21.11 (2018), pp. 1121–1140. DOI: 10.1002/we.2218.
- [5] Gerard V. Ryan, Thomas A. A. Adcock, and Ross A. McAdam. "Soil Masing Behaviour for Offshore Wind TurbinesFatigue Design and a Simple Damping Model". In: *Wind Energy* 28.3 (Feb. 2025). DOI: 10.1002/we.2973. URL: https://onlinelibrary.wiley.com/doi/full/10.1002/we.2973.
- [6] W. Carswell et al. "Foundation damping and the dynamics of offshore wind turbine monopiles". In: *Renewable Energy* 80 (Mar. 2015), pp. 724-736. DOI: 10.1016/j.renene.2015.02.058. URL: https://doi.org/10.1016/j.renene.2015.02.058.
- [7] Dawid Augustyn et al. "Data-driven model updating of an offshore wind jacket substructure". In: Applied Ocean Research 104 (2020). DOI: 10.1016/j.apor.2020. 102366. URL: https://www.sciencedirect.com/science/article/pii/S0141118% 20720309251.
- [8] Shuai Gong, Sau-Lon James Hu, and Hua-Jun Li. "Inverse modeling of damping and soilstructure interface for monopiled offshore wind turbines". In: *Ocean Engineering* 216 (2020). DOI: 10.1016/j.oceaneng.2020.108079. URL: https://doi.org/10.1016/j.oceaneng.2020.108079.
- [9] Xinran Ren et al. "Support condition monitoring of monopile-supported offshore wind turbines in layered soil based on model updating". In: *Marine Structures* 87 (Jan. 2023). ISSN: 0951-8339. DOI: 10.1016/j.marstruc.2022.103342. URL: https://www.sciencedirect.com/science/article/pii/S0951833922001782.
- [10] Mansureh-Sadat Nabiyan et al. "Mechanics-based model updating for identification and virtual sensing of an offshore wind turbine using sparse measurements". In: Structural Control and Health Monitoring 28.2 (2021). First published online: 15 Nov 2020. DOI: 10.1002/stc.2647. URL: https://onlinelibrary.wiley.com/doi/10.1002/stc.2647.
- [11] Singiresu S. Rao. *Mechanical Vibrations*. 6th. Section 2.3. Upper Saddle River, NJ, USA: Pearson, 2017. ISBN: 9780134361307.



- [12] Jan Høgsberg. Dynamics of Structures: theory and analysis. Tech. rep. lecture material, 2D FE modeling Python code by Oscar Bondo Ellekvist. Kongens Lyngby, Denmark: Technical University of Denmark, Department of Mechanical Engineering, June 2020.
- [13] A. J. M. Ferreira and N. Fantuzzi. MATLAB Codes for Finite Element Analysis: Solids and Structures. 2nd ed. Vol. 157. Solid Mechanics and Its Applications. Springer Cham, 2020. ISBN: 978-3-030-47951-0. DOI: 10.1007/978-3-030-47952-7.
- [14] Daniel J. Inman. *Engineering Vibration*. 2nd. International Edition. NJ, USA: Prentice Hall, 2001.
- [15] Mads G. Pedersen. Mass matrix for RNA provided for master thesis. Tech. rep. unpublished material.
- [16] Wikipedia contributors. Viscoelasticity. https://en.wikipedia.org/wiki/Viscoelasticity. (Visited on 04/17/2025).
- [17] Elsevier. Maxwell model. URL: https://www.sciencedirect.com/topics/engineering/maxwell-model (visited on 04/17/2025).
- [18] Elsevier. Kelvin Voigt model. URL: https://www.sciencedirect.com/topics/engineering/kelvin-voigt-model (visited on 03/17/2025).
- [19] Wikipedia contributors. Standard linear solid model. URL: https://en.wikipedia.org/wiki/Standard_linear_solid_model (visited on 04/22/2025).
- [20] C.-Y. Lin et al. "Constitutive Equations for Analyzing Stress Relaxation and Creep of Viscoelastic Materials Based on Standard Linear Solid Model Derived with Finite Loading Rate". In: *Polymers* 14.10 (2022). DOI: 10.3390/polym14102124. URL: https://www.mdpi.com/2073-4360/14/10/2124 (visited on 04/22/2025).
- [21] Elsevier. Maxwell Body. URL: https://www.sciencedirect.com/topics/physics-and-astronomy/maxwell-body (visited on 04/22/2025).
- [22] Steen Krenk. *Dynamics of Structures*. Tech. rep. lecture notes. Kongens Lyngby, Denmark: Technical University of Denmark, Department of Mechanical Engineering, 2018.
- [23] John T. Young. Primer on the Craig-Bampton Method: An Introduction to Boundary Node Functions, Base Shake Analyses, Load Transformation Matrices, Modal Synthesis and Much More. Tech. rep. based on input from William B. Hails. Oct. 2000.
- [24] R. Brincker and C. E. Ventura. *Introduction to Operational Modal Analysis*. Chichester, UK: John Wiley & Sons, 2015.
- [25] C. Rainieri and G. Fabbrocino. Operational Modal Analysis of Civil Engineering Structures. New York, NY, USA: Springer Science+Business Media, 2014.
- [26] Dag Pasquale Pasca et al. pyOMA² Documentation. pyOMA2 Developers. 2025. URL: https://pyoma.readthedocs.io/en/main/ (visited on 06/06/2025).



- [27] Dario Cascone et al. "Influence of User-Defined Parameters Using Stochastic Subspace Identification (SSI)". In: *Proceedings of XXIV AIMETA Conference 2019*. Ed. by Antonio Carcaterra, Achille Paolone, and Giorgio Graziani. Lecture Notes in Mechanical Engineering. First online: 31 March 2020. Springer, Cham, 2020, pp. 1567–1582. ISBN: 978-3-030-41057-5.
- [28] SciPy Community. minimize(method='Nelder-Mead'): SciPy v1.16.0 Manual. 1.16.0. SciPy Developers. 2025. URL: https://docs.scipy.org/doc/scipy/reference/optimize-minimize-neldermead.html (visited on 01/07/2025).



11 Appendices

11.1

11.2 Appendix B: Stabilizing diagram, close up of mode 1 & 2

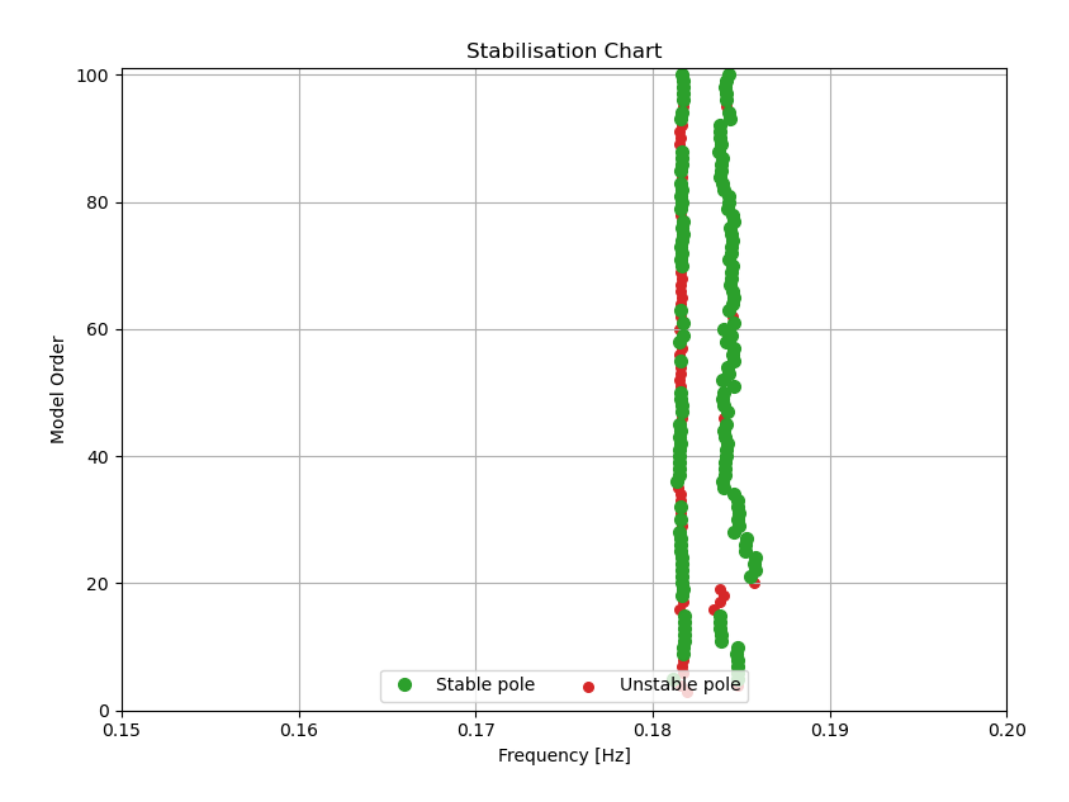


Figure 11.1: Stabilization diagram for frequency across model order, close up for the first two modes.

11.3 Appendix C: Acceleration of tower

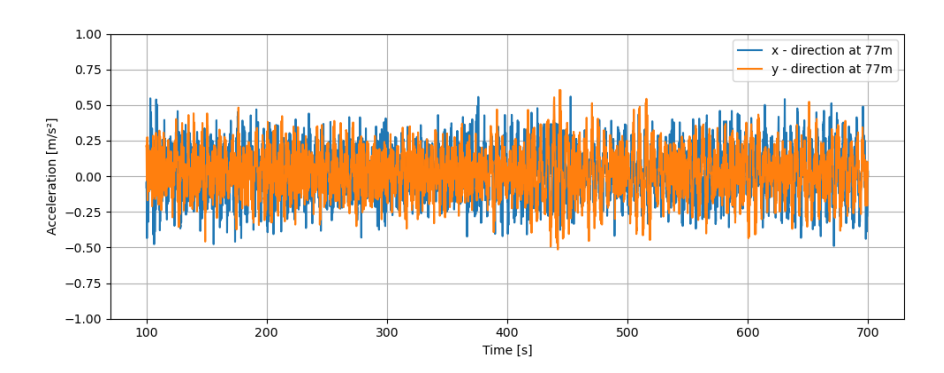


Figure 11.2: Acceleration time series for the top node at the 77m for x and y direction.

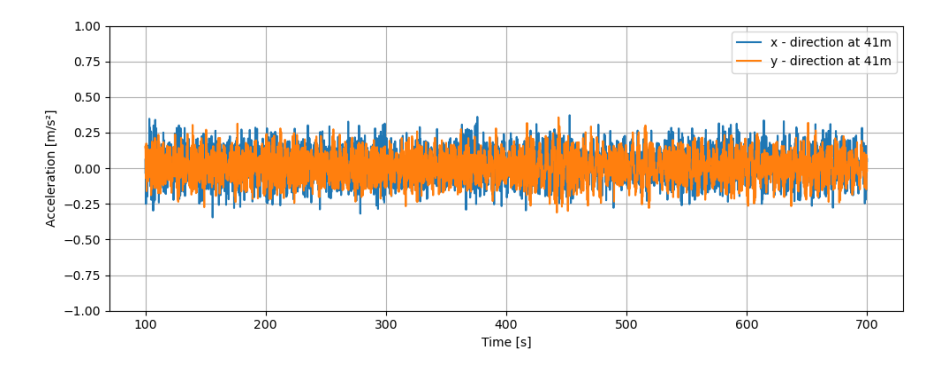


Figure 11.3: Acceleration time series for the top node at the 41m for x and y direction.

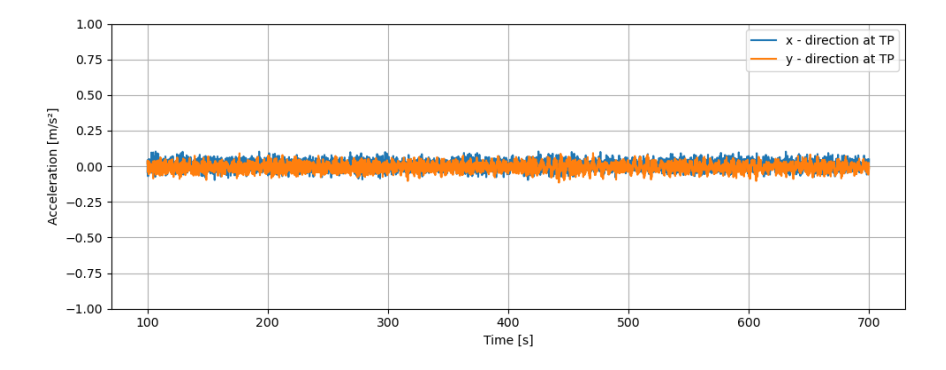


Figure 11.4: Acceleration time series for the top node at the TP for x and y direction.